HHS Public Access

Author manuscript

Cell. Author manuscript; available in PMC 2023 November 23.

Published in final edited form as:

Cell. 2022 November 23; 185(24): 4488–4506.e20. doi:10.1016/j.cell.2022.09.042.

WNK kinases sense molecular crowding and rescue cell volume via phase separation

Cary R. Boyd-Shiwarski[1,8,15], **Daniel J. Shiwarski**[9,15], **Shawn E. Griffiths**[1], **Rebecca T. Beacham**[1], **Logan Norrell**[11], **Daryl E. Morrison**[11], **Jun Wang**[2], **Jacob Mann**[3], **William Tennant**[3], **Eric N. Anderson**[4], **Jonathan Franks**[5], **Michael Calderon**[5], **Kelly A. Connolly**[1], **Muhammad Umar Cheema**[1], **Claire J. Weaver**[1], **Lubika J. Nkashama**[1], **Claire C. Weckerly**[6], **Katherine E. Querry**[1], **Udai Bhan Pandey**[4,7], **Christopher J. Donnelly**[3,7], **Dandan Sun**[2,14], **Aylin R. Rodan**[10,11,12,13], **Arohan R. Subramanya**[1,6,7,8,14,16,*]

[1]Department of Medicine, Renal-Electrolyte Division, University of Pittsburgh School of Medicine, Pittsburgh, PA, 15261, USA

[2]Department of Neurology, University of Pittsburgh School of Medicine, Pittsburgh, PA, 15261, USA

[3]Department of Neurobiology, University of Pittsburgh School of Medicine, Pittsburgh, PA, 15261, USA

[4]Department of Pediatrics, University of Pittsburgh School of Medicine, Pittsburgh, PA, 15261, USA

[5]Center for Biological Imaging, University of Pittsburgh School of Medicine, Pittsburgh, PA, 15261, USA

[6]Department of Cell Biology, University of Pittsburgh School of Medicine, Pittsburgh, PA, 15261, USA

[7]Center for Protein Conformational Diseases, University of Pittsburgh School of Medicine, Pittsburgh, PA, 15261, USA

[8]Pittsburgh Center for Kidney Research, University of Pittsburgh School of Medicine, Pittsburgh, PA, 15261, USA

[9]Department of Biomedical Engineering, Carnegie Mellon University, Pittsburgh, PA, 15213, USA

[*]Correspondence: ars129@pitt.edu.

Author Contributions

Conceptualization, CB-S, DJS, ARS; Methodology, CB-S, DJS, CJD, DS, ARR, ARS; Investigation, CB-S, DJS, SEG, RTB, DEM, LN, LJN, JM, JW, WT, ENA, JF, MC, KAC, CJW, CCW, KEQ, MUC; Resources, UBP, CJD, DS, ARR, ARS; Writing – Original Draft, CB-S, DJS, SEG, RTB., JW, WT, CJD, JF, ARR, ARS; Writing – Review and Editing, UP, ENA, JW, CJW, CCW, DS, ARR, ARS; Supervision, UP, CJD, DS, ARR, ARS; Funding Acquisition, CB-S, DJS, DS, ARR, ARS

Declaration of Interests

The authors declare no competing interests.

Inclusion and Diversity

One or more of the authors of this paper self-identifies as an underrepresented ethnic minority in science.

[10]Department of Human Genetics, University of Utah, Salt Lake City, UT, 84132, USA

[11]Molecular Medicine Program, University of Utah, Salt Lake City, UT, 84132, USA

[12]Department of Internal Medicine, Division of Nephrology and Hypertension, University of Utah, Salt Lake City, UT, 84132, USA

[13]Medical Service, VA Salt Lake City Healthcare System, Salt Lake City, UT, 84148, USA

[14]VA Pittsburgh Healthcare System, Pittsburgh, PA, 15240, USA

[15]These authors contributed equally

[16]Lead Contact

Summary

When challenged by hypertonicity, dehydrated cells must recover their volume to survive. This process requires the phosphorylation-dependent regulation of SLC12 cation chloride transporters by WNK kinases, but how these kinases are activated by cell shrinkage remains unknown. Within seconds of cell exposure to hypertonicity, WNK1 concentrates into membraneless condensates, initiating a phosphorylation-dependent signal that drives net ion influx via the SLC12 cotransporters to restore cell volume. WNK1 condensate formation is driven by its intrinsically disordered C-terminus, whose evolutionarily conserved signatures are necessary for efficient phase separation and volume recovery. This disorder-encoded phase behavior occurs within physiological constraints and is activated in vivo by molecular crowding rather than changes in cell size. This allows kinase activity despite an inhibitory ionic milieu and permits cell volume recovery through condensate-mediated signal amplification. Thus, WNK kinases are physiological crowding sensors that phase separate to coordinate a cell volume rescue response.

In Brief (eTOC Blurb)

WNK1 is a molecular crowding sensor that undergoes cell shrinkage dependent phase separation and restores cell volume. This study provides a clear link between intrinsically disordered region mediated phase-separation of a protein and cell physiology.

Graphical Abstract

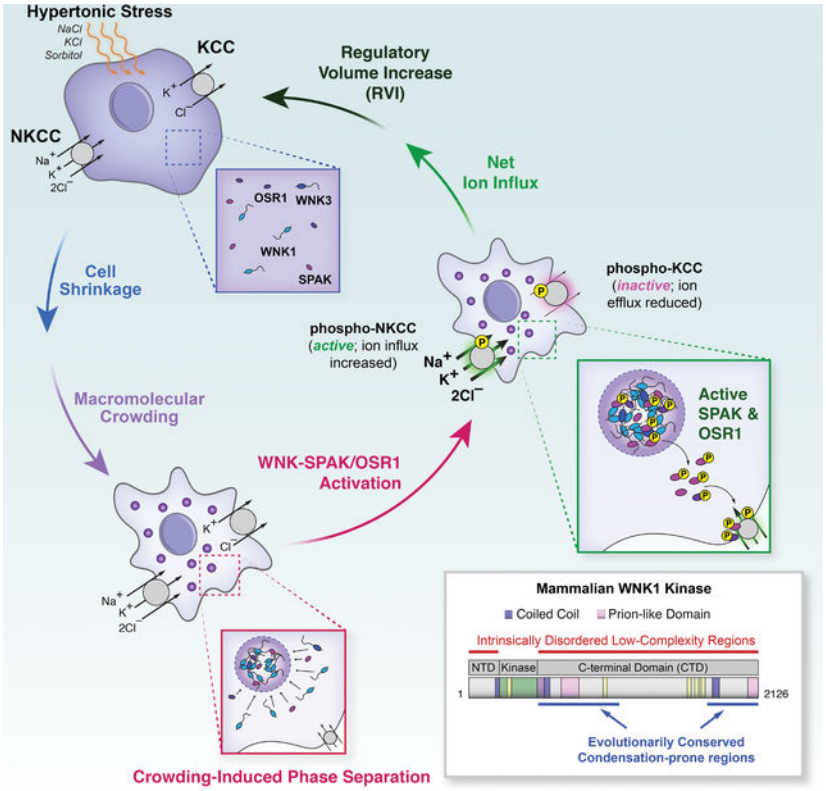

Keywords

WNK Kinase; Hyperosmotic Stress; Cell Volume Regulation; SLC12 Cotransporter; Na-K-2Cl cotransport; K-Cl cotransport; Phase Separation; Condensates; Macromolecular Crowding

Introduction

Eukaryotic cells are constantly subjected to environmental challenges that threaten their fluid volume. During hypertonic stress, cells adapt to volume contraction within seconds by orchestrating a system of ion transporters, channels, and pumps that drive net solute influx, resulting in the obligate reclamation of water (Delpire and Gagnon, 2018). This rapid response, termed regulatory volume increase (RVI), provides a stopgap that gives cells time to synthesize osmolytes and initiate transcriptional programs essential for long-term survival (Burg, 1995). RVI is mediated by specific members of the SLC12 family of electroneutral cation chloride cotransporters (Delpire and Gagnon, 2018). Hypertonic stress activates ion influx via the Na-K-2Cl cotransporter NKCC1; simultaneously, K-Cl cotransporters (KCCs) are inhibited, blocking ion efflux. This results in the net movement of sodium, potassium, and chloride ions into the cell, which stimulates volume recovery. These reciprocal changes in NKCC1/KCC activity are mediated by serine-threonine phosphorylation of the cotransporters via a common signaling cascade that requires With-No-Lysine (WNK) kinases (de Los Heros et al., 2018; Rinehart et al., 2009). Hyperosmotic stress strongly activates the WNKs and deleting WNK kinases from cells

impairs NKCC1/KCC phosphorylation and RVI (Roy et al., 2015b; Zagorska et al., 2007). Thus, WNK kinases play a key role in coordinating volume recovery during hypertonic stress.

To undergo activation by hypertonicity, WNK kinases must first overcome a major obstacle – the increase in intracellular chloride and potassium concentrations experienced by cells during volume contraction (Burg, 1995; O'Neill, 1999). Increases in intracellular ionic strength (including $[Cl]_i$ and $[K+]_i$) potently inhibit WNK kinase activity (Piala et al., 2014; Pleinis et al., 2021). This suggests that an alternate mechanism must be in place that allows the WNKs to sense cell shrinkage, bypass the suppressive effects of ionic strength, and trigger volume recovery via the NKCC1/KCC system.

The mechanisms by which cells detect volume contraction are poorly defined, but likely involve cytoplasmic processes rather than sensors within the plasma membrane (Orlov et al., 2018). Decades ago, investigators proposed that cells adjust their volume not by measuring their cell size *per se*, but rather by monitoring their cytosolic protein concentration (Minton et al., 1992; Parker and Colclasure, 1992). According to this hypothesis, cell shrinkage causes cytoplasmic crowding, which is sensed by signaling pathways that coordinate volume recovery. Crowded intracellular environments may exert such effects by driving the confinement of molecules into compact spaces with altered biochemical activity (Garner and Burg, 1994). For example, macromolecular crowding can induce the formation of biomolecular condensates– functional membraneless microdomains of the cytosol that form via phase separation (PS) (Andre and Spruijt, 2020). Consistent with functional confinement, condensed phases display changes in activity or processing (Sang et al., 2022; Shin and Brangwynne, 2017), and thus could coordinate a sensing mechanism that triggers a response to crowding. Indeed, recent work has implicated PS as a byproduct of hyperosmotic stress (Jalihal et al., 2020). PS can occur on rapid timescales; however, it is unclear if biomolecular condensates mediate rapid physiological responses that occur immediately after stress, such as RVI.

Hypertonicity drives WNK1 into cytoplasmic puncta which have long been assumed to be membrane vesicles (Zagorska et al., 2007). Here, we report the unexpected finding that these structures are biomolecular condensates of the WNK signaling pathway that form via PS. These liquid-like WNK1 droplets assemble within seconds, at physiological levels of hypertonic stress, and at native WNK1 protein concentrations. We identify the large WNK1 C-terminal domain as the primary mediator of PS, map key regions that confer its phase behavior, and confirm its functional relevance by exploring its phylogenesis and effects on downstream pathway activation, ion transport, and RVI. Finally, we show that WNK1 specifically reacts to molecular crowding in vivo, revealing an intrinsic sensing function that allows it to overcome inhibition by chloride and potassium during cell shrinkage.

Results

The WNK-SPAK/OSR1 pathway rapidly assembles into dynamic biomolecular condensates following hyperosmotic stress.

WNK1 is a ubiquitously expressed serine-threonine kinase that controls cell volume (Roy et al., 2015b). During hyperosmotic stress, WNK1 activates, triggering the downstream phosphor-activation of its effector kinases, SPAK (*STK39*) and OSR1 (*OXSR1*), which directly phosphorylate NKCC1 (*SLC12A2*) and the KCCs (*SLC12A4-7*) (Fig 1A) (Zagorska et al., 2007). While NKCC1 phosphorylation by the WNK-SPAK/OSR1 pathway is activating, phosphorylation of the KCCs by the same pathway is inhibitory (de Los Heros et al., 2018). Hyperosmotic stress also shifts WNK1 from a diffuse to punctate cytoplasmic distribution (Fig 1B). This change in localization correlates with NKCC1 activation, KCC inhibition, and RVI (Roy et al., 2015b; Zagorska et al., 2007).

The role of these puncta in WNK signaling has been unclear; thus, we sought to understand their dynamics and functional relevance to the volume recovery response. In live cell imaging studies, transiently expressed mammalian (rat) WNK1 shifted to cytoplasmic puncta with modest hyperosmotic stress (50mM sorbitol; 350mOsm) (Fig 1C), and the foci colocalized with SPAK and OSR1 (Fig 1D), suggesting they physiologically regulate WNK signaling. The puncta were visible with sorbitol stresses as low as 25mM (325 mOsm), and the number of puncta that formed per cell increased with higher degrees of osmotic stress (Fig 1E & 1F). Other hyperosmotic stressors exerted similar effects on WNK1 puncta formation (Fig S1B & S1C). While low Cl-hypotonic stress had no apparent effect on WNK distribution (Fig S1D), a classic “post-RVD-RVI” maneuver (Delpire and Gagnon, 2018), in which cells were returned to isosmotic conditions (300mOsm) following hypotonic swelling led to acute cell shrinkage, which was again associated with WNK1 puncta formation (Fig S1E). This suggests that the WNK1 puncta form in response to relative hypertonic stressors that cause cell shrinkage.

The WNK1 puncta appeared immediately after stress and grew steadily in size, but after 100s, their size stabilized despite a steady decrease in number (Fig 1G). This was associated with the fusion of individual puncta (Fig 1H, Video S1). As the puncta merged, they behaved like liquids, resolved into round structures (Fig 1H and Video S1), wetted against intracellular surfaces (Fig S1F, Video S1), and were membraneless and electron hyperdense in correlative light and transmission electron microscopy (CLEM) experiments (Fig 1I). Collectively, these features are typical of condensates that form via PS. At modest WNK1 expression levels, the puncta underwent nucleation and growth (Fig 1G, 1J, Videos S1 & S2). In cells expressing WNK1 at very high levels, hyperosmotic stress triggered its instantaneous demixing into networks that appeared bicontinuous, consistent with spinodal decomposition (Fig 1J & Video S2) (Shimobayashi et al., 2021). Concentration-dependent nucleation and spinodal decomposition are hallmarks of phase-separating systems (Alberti et al., 2019)

Consistent with dynamic phase behavior, the WNK1 droplets exhibited rapid recovery kinetics in photobleaching experiments (Fig 1K & 1L and Video S1) and dissolved within seconds when the hypertonic stress was quenched with water (Fig 1M). In addition,

changes in WNK1 fluorescence within and outside of the condensed phase were linked, as the reduction in droplet fluorescence during later stages of the post-stress time course was associated with a reciprocal increase in diffuse phase signal (Fig 1N). Thus, condensed material eventually leaves the droplet phase and re-enters the cytosol. In live cell experiments with overexpressed SPAK and WNK1, SPAK mobilized to WNK1 condensates within 15s of hypertonic stress, and by 100s, accumulated at or near the plasma membrane (Fig S1G, Video S3). This finding was not observed when SPAK was overexpressed in the absence of WNK1, indicating that its phase behavior is WNK1 dependent (Fig S1H, Video S3).

Endogenous WNK1 forms hyperosmotic stress-induced condensates.

To determine if these findings are relevant at native levels of WNK1 expression, we first evaluated endogenous WNK1 localization in fixed HEK-293 cells subjected to hyperosmotic stress, using a validated WNK1 antibody (Fig S2A & B). Osmotically stressed cells exhibited high-intensity WNK1 puncta that nucleated above optical diffraction limits (Fig 2A & B) and became larger with increasing degrees of hypertonicity (Fig 2C & D). Similar findings were observed in U2OS and GBM43 glioma cells (Fig S2C). In all three cell lines tested, endogenous WNK1 was occasionally present in small high intensity puncta under isosmotic conditions (Fig 2C, 2D, S2C). This suggests that low-level WNK1 puncta formation could contribute to its endogenous baseline activity during isotonicity.

To assess native WNK1 condensate dynamics, we used CRISPR/Cas9 technology to introduce an in-frame N-terminal mNeonGreen fluorescence tag into the first exon of WNK1 (Fig. S2D). This modification had no effect on WNK1 expression, or on SPAK/OSR1 activation (Fig. S2E). Though the mNG-WNK1 puncta were smaller than those observed during overexpressed conditions, they nucleated seconds after hyperosmotic stress and underwent fusion (Video S4). Like the overexpressed WNK1 condensates, the fusion events resulted in high-intensity mNG-WNK1 puncta that steadily decreased in number but maintained a relatively stable size over a time course of minutes (Fig 2E, F). The mNG-WNK1 puncta also exhibited recovery in FRAP experiments (Fig S2F), though the kinetics were slightly slower than that of the overexpressed WNK1 condensates (Fig 1L). Consistent with a physiologic role in WNK signaling, mNG-WNK1 puncta contained the osmotic stress-responsive paralog WNK3 (Pacheco-Alvarez et al., 2020), SPAK, and OSR1 (Fig 2G). The WNK3 and total and phosphorylated forms of SPAK and OSR1 (pSPAK/pOSR1) signals were 70–80% colocalized with mNG-WNK1 (Fig 2H).

In high resolution colocalization studies with subcellular markers, the mNG-WNK1 puncta did not colocalize with endosomes (EEA1) or lysosomes (LAMP2) (Fig S3A & B). In contrast to an earlier report (Zagorska et al., 2007), we also did not observe colocalization between mNG-WNK1 and the AP-1 adaptor complex. However, consistent with prior work (Pleiner et al., 2021; Zagorska et al., 2007), the stress-induced WNK1 puncta colocalized strongly with clathrin heavy chain (CHC; Fig S3A & B). Hypertonic stress suppresses endocytosis, coated pit formation, and releases CHC from membranes into the cytosol (Hansen et al., 1993; Heuser and Anderson, 1989). Since CHC also physically associates with WNK1 (Pleiner et al., 2021), these findings indicate that WNK1 sequesters

clathrin within membraneless condensates during cell shrinkage. Overexpressed WNK1 also colocalized strongly with CHC during hyperosmotic stress, indicating that the condensates characterized in Figure 1 and natively expressed mNG-WNK1 puncta share the same features (Fig S3C). Further supporting the membraneless nature of mNG-WNK1 puncta, they partially colocalized with EMC2, a soluble subunit of the ER membrane protein complex that binds to WNK1 in the cytosol (Pleiner et al., 2021). Notably, the WNK1 condensates failed to colocalize with TIAR-1, eIF4e, and DCP2 (Fig S3A & B), indicating that they are distinct from stress granules and P-bodies.

The intrinsically disordered C-terminal domain mediates WNK1 phase separation

Homo- and heterotypic molecular interactions drive protein phase behavior (Riback et al., 2020). For example, multivalent interactions between SH3 domains and binding partners harboring proline-rich motifs can trigger PS (Li et al., 2012). Alternatively, PS often requires associations between intrinsically disordered regions (IDRs) of low sequence complexity that contain prion-like domains (PLDs) (Shin and Brangwynne, 2017). WNK1 harbors numerous proline-rich motifs that bind to SH3 and WW domain partners (He et al., 2007; Roy et al., 2015a), and prediction analysis revealed that nearly the entire WNK1 polypeptide sequence outside of the kinase domain is disordered and of low complexity (Fig 3A). This includes the large C-terminal domain (CTD), which harbors two coiled coil domains adjacent to low-complexity PLDs. Thus, WNK1 contains multiple features that may confer its phase behavior.

To screen for regions of WNK1 that are prone to PS, we used an optogenetic approach that takes advantage of the photolyase homology region (PHR) of *Arabidopsis thaliana* Cry2, which transiently self-associates upon exposure to blue light. Fusing a condensation-prone sequence to the Cry2-PHR domain triggers light-inducible phase separation (LIPS) (Figs 3B & 3C) (Mann et al., 2019; Shin et al., 2017). Cry2Olig, an engineered PHR variant, exhibits higher sensitivity to light-induced clustering (Taslimi et al., 2014) (Fig 3B). We screened for regions in WNK1 that undergo strong or weak LIPS by generating WNK1 fragments fused to either the wild-type (WT) PHR domain of Cry2, or to Cry2Olig (Fig 3D). This approach mapped two areas within the WNK1 CTD that underwent LIPS. One fragment encoding the extreme C-terminal end (1770–2126) was strongly prone to phase separation, as both the WT and Cry2Olig fusions underwent LIPS (Fig 3D & 3E). In addition, rare spontaneous puncta were appreciable with the Cry2Olig construct in the dark state, further supporting its highly condensation-prone nature (Fig 3E, arrowheads). A second more proximal region (480–1242) condensed less strongly, as only the Cry2Olig fusion underwent LIPS (Fig 3D & 3E). Notably, both condensation-prone fragments are low complexity IDRs within the WNK1 CTD that contain coiled coil domains and prion-like signatures. Other regions of WNK1, such as the kinase domain (209–479) failed to undergo LIPS in either the WT PHR or Cry2Olig constructs (Fig 3D & 3E).

To evaluate whether the WNK1 CTD mediates osmotic stress-induced PS, we compared the phase behavior of full length WNK1 to two fragments: (1-1242), containing the proximal PS-prone region, and (1-494), which lacks the entire CTD (Fig 3F). Given the strong dependence of phase behavior on protein concentration (Alberti et al., 2019), cells

with similar levels of pre-stress fluorescence were compared. While the 1-1242 construct underwent PS, it failed to efficiently clear from the cytosol, resulting in smaller less well-defined condensates compared to the full-length protein (Fig 3G, Video S5). The 1-494 construct did not visibly phase separate (Fig 3G, Video S5).

To get a better sense of how the phase behavior of these constructs is tied to WNK1 expression levels, we generated in-cell phase diagrams that estimate in vivo PS at different degrees of hyperosmotic stress as a function of pre-stress fluorescence intensity, a surrogate for protein concentration (Fig S4A & B). Both the full-length and 1-1242 constructs formed stress-induced nucleated and spinodal assemblies (Fig S4A). However, compared to full length WNK1, the 1-1242 construct required higher levels of protein expression and hyperosmotic stress to uniformly cross the transition threshold from a diffuse to nucleated state (a phase boundary referred to as the binodal) (Shimobayashi et al., 2021) (Fig S4B & 3H). On the other hand, the spinodal phase boundary (i.e., the threshold at which a protein undergoes spinodal decomposition instead of nucleation) was roughly similar for the two constructs, particularly at hyperosmotic stresses below 400mOsm. Thus, compared to full-length WNK1, the binodal and spinodal curves for the 1-1242 construct were contracted, resulting in a narrowing of the nucleation window within the physiologic range of hyperosmotic stress (Fig 3H). In contrast to these two constructs, the 1-494 fragment did not form visible condensates at any of the osmotic stresses tested, and thus appeared to exist in a one-phase regime.

If WNK nucleation into droplets augments kinase activation, the PS-deficient 1-494 and 1-1242 constructs should exhibit less activation than the full-length protein. To test this, we performed biochemical assessments of the WNK-SPAK/OSR1 pathway at physiologic levels of hyperosmotic stress (350mOsm). To eliminate the influence of endogenous osmotically-responsive WNK kinases, we conducted these studies in WNK1/WNK3 double knockout (DKO) cells (Fig S5A), which exhibit a reduction in baseline and hypertonicity-induced SPAK/OSR1, NKCC1, and KCC phosphorylation relative to unedited controls (Fig S5B). In DKO cells expressing transfected full-length WNK1, 50mM sorbitol triggered immunodetectable phosphoactivation of SPAK/OSR1 and downstream phosphorylation of NKCC1 and KCCs (Fig 3I & 3J). In contrast, there was little to no increase in phosphorylation of SPAK/OSR1, NKCC1, or KCC in DKO cells transfected with the 1-1242 or 1-494 constructs (Fig 3J). Combining these biochemical studies with the live cell imaging data, these results collectively suggest that the entire C-terminal domain is necessary for WNK1 to drive optimal SPAK/OSR1 activation and downstream NKCC1/KCC phosphorylation via PS.

C-terminal coiled-coil domains augment WNK1 phase behavior and activity.

Coiled coil domains (CCDs) are often present within proteins that undergo PS (Ford and Fioriti, 2020). Because CCDs reside within both regions within the WNK1 C-terminal domain that confer its phase behavior (Figs 3A), we sought to determine their importance. CCs are formed by amino acid heptad repeats (denoted by residues *a* through *g*). Positions *a* and *d* define the CC core (Fig 4A) and are frequently occupied by hydrophobic residues, or by “ambivalent hydrophobes” such as glutamine (Fiumara et al., 2010; Sodek et al., 1972).

Hydrophobic and glutamine residues were present in the *a* and *d* registers of both C-terminal WNK1 CCDs (Fig 4B). In the C-terminal CC (CT-CC), the *a-d* frame also contained a known "HQ" signature which facilitates WNK-WNK interactions (Thastrup et al., 2012). We substituted prolines into these predicted key residues to disrupt CC periodicity without influencing regional disorder tendency (Fig 4B & 4C). This allowed us to specifically evaluate the CCDs independently of IDR function.

Optogenetic assessment of phase separating WNK1 fragments containing the CCDs revealed no effect of the proline mutations on LIPS (Fig 4D). However, in comparative in-cell phase diagrams, a full-length double mutant construct containing proline substitutions in both the MidCC and CTCC (WNK1-CC^{mut}; Fig 4C) exhibited a rightward shift of the binodal phase boundary (Fig 4E). Furthermore, in WNK1-CC^{mut} expressing cells that formed WNK condensates, disruption of the C-terminal CCDs resulted in smaller short-lived puncta. Consistent with reduced WNK1 retention within condensates, this was associated with higher fluorescence intensity in the diffuse phase (Fig 4F). Thus, mutation of the CCDs impaired WNK1's ability to efficiently form large droplets that increase in size and decrease in number as they extract material from the diffuse phase and fuse. In comparative immunoblots with full length WT-WNK1, CCD disruption impaired downstream SPAK/OSR1, NKCC1, and KCC phosphorylation (Fig 4G & 4H). Collectively, these findings indicate that though the C-terminal CCDs are not necessary for PS, they facilitate optimal WNK1 nucleation and pathway activation within condensates.

Phase behavior of the WNK1 CTD is evolutionarily conserved despite poor sequence identity

We wondered if the disorder features present in rat WNK1 are present in other WNK kinases. Thus, we analyzed four WNKs with poorly alignable sequences outside of the kinase domain that mediate similar functions with regards to osmotic stress responsiveness and/or ion transport: human WNK1 (hWNK1), human WNK3 (hWNK3), *Drosophila melanogaster* WNK (dmWNK), and *Caenorhabditis elegans* WNK (ceWNK). Despite their poor sequence identity, the disorder tendency plots and PLDs for these WNKs are nearly identical (Fig 5A). To further explore sequence relationships in WNK IDRs that likely exhibit phase behavior, we analyzed the amino acid composition of WNK CTDs across evolution, extending from humans to protists (Fig S6). Mammalian WNK kinases are enriched in prolines and serines, which comprise approximately 25% of the amino acids in the disordered CTD. This compositional bias extends to freshwater vertebrate fish. However, in many organisms extending from invertebrates down to protists, glutamine is the preferred amino acid. Glutamine and serine regulate the material properties of condensates in a similar manner (Wang et al., 2018). Thus, the WNK CTD underwent a permissive Q-to-P/S switch in compositional bias during early vertebrate evolution that conserved its regional disorder tendency, likely to preserve its phase behavior. This suggests that the ability of WNK kinases to form condensates is an ancient, fundamental property.

To test this further, we turned to the *Drosophila melanogaster* WNK kinase. dmWNK is a central regulator of ion transport in the Malpighian tubule (MT), an ancient but conserved model of the mammalian nephron (Rodan, 2018). Within this system, dmWNK triggers

NKCC phosphoactivation via the SPAK homolog Fray. While the rat WNK1 CTD bears a P/S-rich composition present in other mammalian WNKs, the dmWNK CTD is Q-enriched, as is the case for many invertebrates (Fig 5B). These glutamines cluster in poly-Q tracts that reside in the proximal and distal regions of the C-terminal domain – PLDs that correspond to regions in rat WNK1 that were identified to be critical for PS (Fig 5B). Though poly-Q prion-like sequences are classically considered to be mediators of pathological protein aggregation, they can facilitate physiological stress-induced phase transitions (Franzmann et al., 2018).

Given these observations, we asked whether dmWNK phase separates during hyperosmotic stress. In live cell imaging studies in *Drosophila* S2 cells overexpressing GFP-tagged dmWNK, the full-length construct (1-2253) behaved similarly to mammalian WNK1, shifting to condensates during hyperosmotic stress (Fig 5D). A deletion analysis confirmed that like rat WNK1, dmWNK harbors two zones within its CTD that are primarily responsible for its phase behavior. One of these (846–1000) is a Q-rich region in the middle of the protein that harbors a CCD, while the other is contained within the more distal region of the CTD (1001–2253) (Fig 5C & D). While a dmWNK fragment lacking this distal region (1–1000) still formed condensates (Fig 5D), it exhibited PS in fewer cells compared to the full-length protein at a given level of osmotic stress (Fig 5E). Thus, like mammalian WNK1, the entire disordered CTD is required for optimal PS. These findings reinforce evidence that WNK phase behavior is highly conserved and encoded within specific regions of the CTD.

The WNK1 CTD is required for NKCC1 transport and RVI

To determine whether the WNK1 CTD influences RVI, we performed live cell volume measurements using resonant scanning confocal microscopy. RVI is classically mediated by two processes: cariporide-sensitive coupled sodium/proton and chloride/bicarbonate exchange and bumetanide-sensitive NKCC1/KCC transport (Fig 6A) (Hoffmann et al., 2009). To rule out compensation by the sodium/proton exchanger NHE1, all volume measurements were conducted in the presence of cariporide. Following exposure to 50mM sorbitol, cells expressing full-length rat WNK1 on a WNK1/WNK3 DKO background exhibited a rapid reduction in cell volume (Fig 6B). Notably, the degree of relative volume contraction in DKO cells expressing the 1-494 construct was less than that of DKO cells expressing full length WNK1 (Fig 6B & C). This was associated with baseline differences in cell size. As shown in Fig 6D, 2d post-transfection, DKO cells expressing WNK1 1-494 were 15–20% larger than those expressing full length WNK1. This suggests that cells expressing the 1-494 construct adapt to low baseline WNK activity by maintaining a larger size during the 48h window following transfection. Since cells expressing WNK1 1-494 are larger, their percent volume reduction in response to a given hypertonic stress is less compared to smaller cells expressing full-length WNK1.

To account for the differences in acute volume reduction in cells expressing full length vs 1-494 WNK1, RVI was defined as percent volume recovery, expressed relative to the volume lost (see STAR methods). In cells expressing full-length WNK1, volume contraction was followed by a linear recovery over time, consistent with classical RVI (Fig 6B & E). In contrast, cells expressing the CTD-deficient 1-494 construct exhibited sluggish RVI

following acute cell shrinkage (Fig 6E). In cells expressing full-length WNK1, preincubation with the NKCC1 inhibitor bumetanide blunted the RVI response within the first five minutes of the recovery time course (Fig 6F). In contrast, cells expressing WNK1 1-494 exhibited similar RVI curves in the presence and absence of bumetanide (Fig 6G). Thus, DKO cells expressing the full-length WNK1 construct mounted a bumetanide-sensitive NKCC1-mediated RVI response, while cells expressing the PS-deficient 1-494 construct did not (Fig 6H).

Next, we evaluated the truncated WNK1-1-1242 (Fig 6I & J) and the WNK1-CC^{mut} coiled-coil domain mutant constructs (Fig 6K, & L). In both cases, volume recovery was significantly impaired within the first 5 min post-stress, though the defective RVI responses were less severe than those observed in cells expressing the fully PS-deficient 1-494 construct (Fig 6M). Since the 1-1242 and CC^{mut} constructs exhibited PS phenotypes that were only partially defective, these findings indicate that WNK1-mediated RVI correlates with its phase behavior.

To determine the functional importance of the disordered WNK1 CTD on NKCC1 transport, we measured influx of the K+ congener rubidium (Rb+) under isotonic and hypertonic conditions in WNK1/WNK3 DKO cells expressing full length or 1-494 WNK1. Consistent with the low NKCC1 phosphorylation status in WNK1/WNK3 DKO cells (Fig S5B), in the absence of transfected constructs, the DKO cells exhibit low bumetanide-sensitive Rb+ flux, both at baseline and during hypertonic stress (Fig S5C–E). However, we also found that they exhibit increased ouabain-sensitive (Na+/K+ ATPase-mediated) Rb+ influx, suggesting that the DKO cells increase pump activity to compensate for the chronic absence of NKCC/KCC phosphorylation caused by WNK1/WNK3 deletion (Fig S5C–E). For this reason, we focused on bumetanide-sensitive fluxes for these experiments. A shift in osmolality from near isotonicity (310 mOsm) to hypertonicity (370 mOsm) was associated with greater shrinkage-induced bumetanide-sensitive Rb+ influx in DKO cells expressing full-length WNK1 compared to 1-494 WNK1 (Fig 6N & O).

Orthogonal replacement of the WNK1 CTD rescues RVI

Our deletion and coiled-coil mutant analyses demonstrate that the WNK CTD mediates PS and is critical for RVI following cell shrinkage (Fig 3, 4, 6). However, these studies do not uncouple PS from other potential functions encoded within the CTD that may be critical for RVI. To determine whether WNK kinase phase separation *per se* mediates RVI, we replaced the WNK1 CTD (residues 495–2126) with orthogonal disordered domains from two unrelated proteins known to confer PS. The first of these chimeras contained the N-terminal 267 amino acids of fused in sarcoma (FUS), while the second contained residues 274–414 of TAR-DNA binding protein 43 (TDP-43) (Fig S7A & S7B). Both domains are well-studied intrinsically disordered LCRs that drive PS (Portz et al., 2021). Since these domains were fused to a truncated WNK1 construct that does not phase separate but contains a fully intact active kinase domain, this allowed us to test whether PS of the WNK1 kinase domain is sufficient to trigger an RVI response. The WNK1 1-494-FUS and 1-494-TDP-43 chimeras underwent PS within seconds of exposure to 50mM sorbitol (Fig S7C, Video S6), and live cell coexpression studies revealed that SPAK partially colocalized with

the chimeras in condensates (Fig S7D). In RVI experiments, both the WNK1 1-494-FUS and 1-494-TDP-43 chimeras mediated volume recovery more efficiently than 1-494 alone (Fig 6M, S7E, & S7F). Surprisingly, the 1-494-TDP-43 construct rescued volume almost as efficiently as the full-length WNK1 protein (Fig S7F). Collectively, these data demonstrate that PS of the WNK1 kinase domain is sufficient to mediate RVI.

WNK1 is a molecular crowding sensor

Macromolecular crowding commonly triggers protein phase separation and has also been proposed to be a stimulus for RVI (Andre and Spruijt, 2020; Colclasure and Parker, 1991; Delarue et al., 2018). Thus, we hypothesized that the formation of bioactive WNK1 condensates may be the manifestation of a crowding-sensing mechanism that triggers the RVI response. To test this, we designed an experiment that augments cytoplasmic molecular crowding without causing cell shrinkage. Ficoll is a molecular crowding agent that is commonly used to trigger protein PS in vitro (Andre and Spruijt, 2020). We reasoned that cytoplasmic Ficoll microinjection should increase the degree of cytosolic crowding while simultaneously increasing cell size. If a protein phase separates under such conditions, it could be reasoned that it does so because of molecular crowding rather than shrinkage (Fig 7A).

As a first approach, we used mNG-WNK1 cells, which express WNK1 at native levels. As noted in Fig 2E, these cells exhibit low-grade WNK1 condensation under isotonic conditions, resulting in a granular appearing cytoplasm with partial localization of mNG fluorescence in small puncta (Fig 7B). Following the microinjection of a control vehicle buffer lacking crowding agent, cells expanded and the mNG signal became diffuse and homogeneous, consistent with condensate dissolution due to cytoplasmic dilution (Fig 7B). In contrast, Ficoll microinjection triggered the formation of large WNK1 condensates which extracted WNK1 from the surrounding dilute phase (Fig 7C). Introduction of Ficoll into swollen cells that were precleared of puncta by hypotonic stress was associated with the localized collection of long-lived condensates that grew near the injection site over time (Fig 7D & 7E).

We also conducted injection studies in wild-type HEK-293 cells overexpressing mRb2-tagged WNK1 constructs. In cells expressing full length WNK1, cytosolic Ficoll injection triggered widespread condensate formation (Fig 7F, Video S7). In contrast, the 1-494 WNK1 fragment did not phase separate following cytosolic injection. Instead, it remained diffuse and its cytosolic fluorescence intensity decreased, likely due to signal dilution caused by an increase in cell size following microinjection (Fig 7G, Video S7). In contrast to full length WNK1, whose subcellular distribution is restricted to the cytosol, the truncated 1-494 construct partially distributes in the nucleus, and the fluorescence intensity of the nuclear fraction remained relatively constant throughout the course of the experiment. These findings demonstrate that in vivo WNK1 phase separation is due to changes in cytoplasmic crowding rather than cell size. These findings therefore implicate WNK kinases as intracellular molecular crowding sensors that utilize PS as a mechanism to control cell volume.

Discussion

WNK kinases have long been appreciated to participate in cellular osmosensing, but the mechanisms by which they activate downstream signaling following volume contraction have been obscure. In this work, we show that WNK1 responds to hyperosmotic stress by detecting a crowded cytosol. It does so by undergoing PS, forming functional condensates that activate the WNK-SPAK/OSR1 pathway to trigger downstream NKCC1/KCC phosphorylation, net ion influx, and RVI (Fig 7H). WNK1 phase behavior occurs within physiological constraints and is mediated by its large CTD, which is highly conserved with respect to its size, regional disorder tendency, and domain organization despite poor sequence identity across evolution. These features allow even the most ancient WNKs to quickly detect small changes in hypertonicity. Taken together, our results reveal an evolutionarily conserved function for WNK kinases as physiological crowding sensors and identify WNK1 as a key constituent of a multicomponent signaling condensate that manages acute reductions in cell volume.

The theory of macromolecular crowding as a cell volume signal and as a stimulus for cytoplasmic PS was proposed decades ago (Parker, 1993; Walter and Brooks, 1995; Zimmerman and Harrison, 1987). These concepts were underappreciated; however, a paradigm shift in our understanding of cytoplasmic organization has prompted their reappraisal (Hyman et al., 2014). Hypertonicity diminishes solvation of the cytosol, creating an ideal milieu for interactions between multivalent proteins that are prone to phase behavior. This suggests that crowding-induced PS caused by hyperosmotic stress broadly modulates the activity of biomolecules that tend to form condensates (Jalihal et al., 2020).

The ability of WNK1 to activate in response to crowding addresses a longstanding paradox in the WNK signaling field. As shown here, the WNK-SPAK/OSR1-NKCC pathway is upregulated by hypertonicity; however, intracellular Cl^- and K^+ depletion are also potent WNK activators (Piala et al., 2014; Pleinis et al., 2021). These observations have been difficult to reconcile, as hypertonic stress raises intracellular ionic strength due to exosmosis (O'Neill, 1999). Because this elevation in intracellular Cl^- and K^+ concentrations should inhibit WNK kinase activity, the stimulatory effects of hypertonicity seem counterintuitive. Our results provide evidence that the crowding-dependent condensation of WNK kinases allows them to activate while bypassing the inhibitory effects of high ionic strength caused by cell water loss.

WNK kinases harbor a large intrinsically disordered C-terminal domain, usually greater than 100 kilodaltons in mass, whose function has been incompletely understood. Our studies show that the entire domain is critical for WNK1 to undergo PS in response to modest reductions in cell volume. The WNK CTD can therefore be thought of as a physiological crowding sensing domain. Though the sequence identities of WNK CTDs vary widely across evolution, their regional features in terms of disorder, low complexity, and prion-like signatures share striking similarities. In mammalian WNK1, regions at both the proximal and distal ends of the CTD are particularly prone to phase behavior, and coiled-coil domains within these regions augment kinase retention within the condensed phase to optimize downstream SPAK/OSR1 activation. Moreover, deletion of the distal end of the CTD

impairs condensate formation, reducing the sensitivity of WNK1 to crowding. Analysis of the *Drosophila* WNK CTD suggests that these features are evolutionarily conserved. Thus, it appears that the large size of the CTD is a conserved feature that allows WNK kinases to react to physiologic changes in cytosolic crowding. These findings have implications for understanding how IDRs mediate physiological sensing functions in vivo.

Our findings have broad implications for WNK-dependent signaling in health and disease, as the mechanisms that mediate RVI have been leveraged by higher organisms to control advanced physiologic processes. For example, mutations in the WNK signaling pathway cause hypertension and hyperkalemia due to the overactivation of NCC, an NKCC1-like SLC12 salt cotransporter localized to kidney distal convoluted tubule (DCT) (Subramanya and Ellison, 2014). Within this nephron segment, WNK activation is associated with the formation of DCT-specific biomolecular condensates called WNK bodies (Boyd-Shiwarski et al., 2018). The assembly of these membraneless structures is driven by KS-WNK1, a truncated WNK1 isoform that retains the entire disordered CTD shown here to be critical for PS. This suggests that KS-WNK1 scaffolds WNK-dependent phase transitions that participate in volume and K+ homeostasis. NKCC1-dependent transport contributes to colonic epithelial K+ secretion (Nickerson and Rajendran, 2021), choroid plexus function (Steffensen et al., 2018), and ischemic stroke (Bhuiyan et al., 2016); these processes likely require WNK phase behavior. Furthermore, drugs targeting the WNK-SPAK/OSR1 pathway may influence condensate dynamics. ZT-1a, a potent small molecule SPAK inhibitor, disrupts interactions with WNK1 and mitigates ischemic injury following stroke (Zhang et al., 2020). It would be of interest to evaluate whether ZT-1a modulates condensate-dependent WNK signaling, as this may have implications for future therapeutics for the WNK-SPAK/OSR1 pathway, and for condensate drug design in general.

PS has emerged as a fundamental property of biomolecules that is reshaping theories regarding cellular organization. However, protein phase behavior is often only loosely connected to physiological relevance (Leslie, 2021; McSwiggen et al., 2019). Our results provide evidence that PS of the WNK signaling pathway is functionally relevant, occurring at native protein concentrations and at levels of osmotic stress that are within a physiological range commonly experienced during life. Many of the biophysical principles regarding the inherent molecular features of phase separating systems are evolutionarily encoded within WNK kinases to link condensate formation to cell volume regulation. Thus, the results presented here provide strong support for the relevance of biomolecular condensates in cellular physiology.

Limitations of the study

Some of our live cell experiments were conducted with eGFP tagged constructs. Since eGFP is weakly dimeric, this might have influenced condensate dynamics. Though WNK1 activates within condensates, how it does so remains an open question. In vitro evidence suggests that hyperosmotic stress triggers WNK autoactivation via dehydration of the kinase domain (Akella et al., 2021). Since condensed phases provide alternate solvent environments (Nott et al., 2015), they may be an ideal location for this process to occur. Due to the lack of suitable phosphoantibodies, however, we were unable to directly measure

WNK autoactivation. Our data indicate that following condensation, the WNK-SPAK/OSR1 pathway eventually re-enters the cytosol. We did not investigate how this occurs, though it seems likely that phosphorylation of signaling molecules within condensates is involved. Alternatively, co-regulators of the WNK-SPAK/OSR1 pathway may be required. For example, kinases such as ASK3 (Watanabe et al., 2021), mTOR (Demian et al., 2019), p38 (Liu et al., 2022), and protein kinase C (Li et al., 2004), or volume regulated channels such as LRRC8 (Serra et al., 2021), may influence the WNK-SPAK/OSR1 pathway within or outside of condensates and would be ideal candidates to evaluate in future studies.

RESOURCE AVAILABILITY

Lead Contact—Further information and requests for all resources and reagents in this study should be directed to and will be fulfilled by the lead contact, Arohan Subramanya (ars129@pitt.edu).

Materials Availability—All unique reagents in this study are available from the Lead Contact and will be provided upon request.

Data and Code Availability

- Data including additional supplemental videos and tables have been deposited at Mendeley and are publicly available as of the date of publication. DOI is listed in the key resources table.
- This paper does not report original code.
- Any additional information required to reanalyze the data reported in this paper is available from the lead contact upon request.

EXPERIMENTAL MODEL AND SUBJECT DETAILS

Cell lines—HEK-293 and U2OS cells (both human, female) were cultured in a 37-degree 5% CO_2 incubator in complete media (glucose-supplemented DMEM with 10% FBS, L-glutamine, and penicillin/streptomycin). All HEK-293 cell lines are tested for mycoplasma contamination quarterly. GBM43 cells (human, male) were cultured in a 37-degree CO2 incubator in Neurobasal media supplemented with B27-A and N2 (ThermoFisher), basic FGF, EGF, L-glutamine, and penicillin/streptomycin. *Drosophila* S2-Gal4 cells (male; provided by Dr. Adrian Rothenfluh) (Acevedo et al., 2015) were maintained at 26°C, in Schneider's Drosophila media supplemented with 10% Fetal Bovine Serum (ThermoFisher Cat. No 21720024).

Mice—Global NKCC1 KO mice (Flagella et al., 1999) and littermate controls, used only for antibody validation, were housed in a temperature-controlled room on a 12h light/dark cycle, with free access to standard diet and deionized water. Tissue from one adult male KO mouse and one adult male littermate control were used for analysis. Mice were 3–4 months of age at the time of analysis. All animal protocols related to care, sacrifice, and organ harvest conformed to the NIH Guide for the Care and Use of Laboratory Animals, and were approved by the University of Pittsburgh IACUC.

METHOD DETAILS

Plasmid Construction—All mammalian WNK1 clones used for this study were derived from the original untagged rat WNK1 cDNA (AAF74258.1), which encodes a 2126 amino acid kinase-active isoform isolated from brain (Xu et al., 2000). This cDNA was modified to correct a variant serine present in residue 2120 of the original cDNA back to a conserved glycine to match the canonical Uniprot sequence Q9JIH7-1, and subcloned into the *EcoRI* and *XbaI* sites of pcDNA3.1. In the Key Resources Table, this complete CDS is referred to as rWNK1-S-G, but is referred to as "full-length WNK1" in this study. C-terminal eGFP-tagged WNK1 was reported previously (Boyd-Shiwarski et al., 2018). To generate N-terminal mRuby2-tagged WNK1, a gBlock encoding mRuby2 fused to the WNK1 N-terminus via a GRGS linker was synthesized (IDT) and swapped with an *EcoRI*/*NotI* N-terminal fragment in WNK1. Truncated N-terminal mRb2 tagged 1-494 and 1-1242 fragments constructs were generated by PCR off the full-length template and ligation to linearized pcDNA3.1. The WNK1 1-494-FUS and 1-494-TDP-43 LCR chimeras were generated by amplifying cDNAs encoding residues 1–267 of FUS or residues 274–414 of TDP-43 from previously reported templates (Mann et al., 2019) and ligating them in frame to N-terminally tagged mRuby2-1-494 WNK1 in pcDNA3.1. To generate the double coiled-coil mutant, two gBlocks encoding proline substitutions in the mid and distal coiled coil domains were swapped in stepwise fashion with corresponding regions into the full length mRuby2-WNK1 construct in pcDNA3.1 via restriction cloning. To generate fluorescently tagged SPAK constructs, full-length murine SPAK cDNA (NM_016866.2) was amplified and subcloned to pcDNA3.1, and in-frame N-terminal eGFP or mRuby2 tags were PCR amplified and ligated by restriction cloning. For the Cry2 plasmids, WNK1 fragments were generated by PCR or as synthetic gBlocks and were ligated via restriction cloning to the *XmaI* site of linearized Cry2PHR or Cry2Olig (E490G) vectors (Addgene #26866 and #60032), positioned in-frame between the PHR domain and mCherry.

For the dmWNK constructs, a gBlock encoding *Drosophila* codon-optimized human kinase-dead SPAK (HsSPAK^{D210A}) was synthesized and inserted into the multicistronic vector pAc5 STABLE2 Neo, which contains a GFP cassette (Gonzalez et al., 2011) (Addgene #32426), by Gibson assembly to generate pAc5-GFP:T2A:HsSPAK^{D210A}. dmWNK fragments were then PCR amplified from a full-length clone (Wu et al., 2014) and inserted into this vector in-frame with the GFP cassette by Gibson assembly to generate a series of N-terminal GFP-tagged dmWNK truncation constructs. To delete WNK1 from HEK-293 cells, we used a previously reported bicistronic PX330 plasmid (Addgene #42230) harboring the Cas9 CDS and a single guide RNA (sgRNA) targeting exon 1 of WNK1 (Roy et al., 2015b).

To generate the Cas9/WNK3-sgRNA plasmid, a 20bp guide sequence (WNK3.5) targeting exon 1 of human WNK3 was ligated to the *BbsI* site of PX330 (PX330-WNK3.5). To confirm WNK3 sgRNA efficacy, a complementary pair of 30bp oligonucleotides spanning the WNK3.5 sgRNA target cut site were ligated to a pHRS reporter plasmid (PNABio) (Pereira et al., 2016). To generate mNeonGreen WNK1 knock-in cells, a 20bp guide sequence targeting the 5' end of WNK1 exon 1 was ligated to the *BbsI* site of PX459 (Addgene #62988). In addition, we generated a plasmid harboring a homology-directed

repair knock-in template by inserting the mNeonGreen CDS and 5' and 3' homology arms flanking the WNK1 insertion site into pUC18 via overlap extension PCR and Gibson assembly. The homology arms were amplified from extracted HEK-293 cell genomic DNA (QuickExtract DNA extraction solution, Lucigen). The fidelity of all constructs was confirmed by Sanger or Nanopore sequencing prior to use.

Cell transfection—For HEK-293 and U2OS cells, plasmids were transfected using Lipofectamine 3000 (ThermoFisher) per manufacturer instructions. If transfected cells were used for imaging, they were re-plated on coverslips or MatTek dishes 24h post-transfection. For S2-Gal4 cells, *Drosophila* constructs were transfected with plasmid DNA using TransIT®-Insect transfection reagent (Mirus Bio).

Gene edited cell lines—WNK1/WNK3 double knockout (DKO) HEK-293 cells were generated via methods similar to (Roy et al., 2015b). Cells were grown in 6-well dishes, cotransfected with WNK1-PX330 plasmid and pEGFP-N1, used as a fluorescent marker for sorting transfected cells. 48h later, cells were harvested in PBS + 2% FBS, dilutely sorted into 96-well plates using a FACSAria II cell sorter (BD Biosciences), and clonally expanded. Knockout clones were identified by immunoblotting with validated WNK1 antibodies (Figure S2 and (Boyd-Shiwarski et al., 2018)). To knock out WNK3, the WNK3.5 sgRNA was first functionally validated using a surrogate reporter method (Pereira et al., 2016; Ramakrishna et al., 2014). PX330-WNK3.5 was cotransfected into HEK-293 cells with pHRS-WNK3.5, a reporter plasmid that harbors an out-of-frame GFP cassette 3' to the target cut site. On-plasmid CRISPR-mediated nonhomologous end-joining (NHEJ) shifts the GFP CDS in-frame, resulting in green fluorescence, which was confirmed for cells expressing the WNK3.5 sgRNA by epifluorescence microscopy 48h post transfection. The PX330-WNK3.5 plasmid was then used to knock out WNK3 from WNK1 KO cells using methods identical to those described for WNK1 deletion.

To generate endogenous mNG-tagged WNK1 cells, PX459-WNK1, encoding Cas9 and WNK1-sgRNA, was cotransfected with the pUC18-WNK1/mNeonGreen homology directed repair template plasmid. 72h post-transfection, cells were sorted by FACS for mNeonGreen fluorescence, plated dilutely into 96-well plates, and clonally expanded. Individual clones were validated by immunoblotting for WNK1 and the mNG tag, and by amplification of the target site across the 5' and 3' homology arms by genomic PCR, TA cloning into pGEM-Teasy (Promega), and Sanger sequencing.

Antibodies—To generate the guinea pig total NKCC1 antibody, we targeted amino acids 929–999 of mouse NKCC1 (NCBI NP_033220.2; CCDS 37826.1). This epitope is contained within a unique loop of the NKCC1 C-terminus, and is distinct from sequences in other SLC12 cotransporters, including the closely related NKCC2 (*SLC12A1*) (Carmosino et al., 2008). A fusion protein encoding the NKCC1 epitope fused to GST was expressed by IPTG induction in BL21 E.coli, purified using a HiTrap glutathione S-Transferase column, and eluted with 10mM reduced glutathione. The free glutathione was removed by overnight dialysis and purity was confirmed by SDS-PAGE. Antibody production in guinea pigs was carried out by Pocono Rabbit Farm and Laboratory (Canadensis, PA). Validation of the antibody in global NKCC1 KO mice (Flagella et al., 1999) is shown in Figure S1A. We were

unable to detect phosphorylated NKCC1 using several commercial antibodies; therefore, we used a previously validated antibody that was directed to phosphorylated Threonine-58 of NCC (*SLC12A3*) (Sorensen et al., 2013). The epitope recognized by this antibody (amino acids 54–62 of mouse NCC; FGHYNpTIDVV) cross-reacts with a phospho-activation site present in mouse NKCC2 and NKCC1 (Gimenez and Forbush, 2003; Lee et al., 2013). Phosphorylation at this site is a signature of NKCC activation (Flemmer et al., 2002); thus, the pT58 antibody was used to provide a readout of activated NKCC1 in HEK-293 cells. TIAR was detected using a previously reported antibody (Daigle et al., 2016).

Live cell imaging of WNK condensates—HEK-293 cells were plated in 6-well dishes in complete media and allowed to grow to 80–90% confluency. Cells were transfected in antibiotic-free media the following day with standardized amounts of mRuby2 tagged WNK1 plasmids. Cells were re-plated 24h post-transfection on poly-D-lysine coated MatTek dishes. Tonic solutions and media were prepared and warmed to 37°C on the day of imaging. Cell media was replaced with Leibovitz L-15 media and dish was loaded into a climate-controlled stage set to 38°C of a Leica SP8 live cell resonant scanning confocal microscope using a Leica HC Pl APO CS2 63X, 1.40 numerical aperture oil objective. Scan speed was set to 1000 Hz and images were captured in a 2048×2048 resolution format. Cells were screened and selected for imaging with similar mRuby2 signal intensities to evaluate condensate behavior in cells with relatively equal amounts of WNK1 protein by taking an intensity measurement in Fiji prior to imaging. Stress media (50 mM sorbitol) was added after the second stack was taken to establish a pre-stress baseline. Confocal stacks (10–18 steps, 1μm step size) capturing mRuby2 signal were taken every 15 seconds for 10 minutes.

Spinning disk confocal fluorescence live cell imaging was performed on a Nikon Ti-E-2000 inverted microscope equipped with an Andor Revolution XDi spinning disk, a 100X objective (Nikon CFI Plan Apo TIRF Lambda, 1.49 NA), Piezo XYZ stage (Nikon), iXon 897 Ultra back-illuminated camera (Andor Technology), a laser combiner (Andor Technology) containing 405, 488, 515, 568, and 647 nm excitation capabilities, Perfect Focus system (Nikon), a Dell 5400 Workstation with IQ2 imaging software (Andor Technology), and an active isolation air table (TMC) (Shiwarski et al., 2019). The system was surrounded by a full heated enclosure to maintain physiological temperature and humidity. eGFP and mRuby WNK1 expressing cells were grown on coverslips and transferred to a metal imaging chamber (AttoFlour, Invitrogen) in Leibovitz's L-15 media + 1% FBS. eGFP and mRuby were imaged using 488 nm laser excitation with 525/50 nm emission filter, and 561 nm laser excitation with 620/60 nm emission filter, respectively. Exposure duration, laser power, camera gain, and Z-step sizes were optimized to achieve fast 3D imaging at Nyquist resolution of WNK1 condensate formation while minimizing photobleaching during the time-lapse imaging. 3D rendering of the image stacks were performed using the IQ2 built-in animation features and Imaris software (Bitplane).

For live cell imaging in *Drosophila* S2-Gal4 cells, 48 hours following transfection, cells expressing GFP-dmWNK constructs were resuspended and transferred in 500 μl aliquots to 1.5mL centrifuge tubes. The cell suspension was then diluted stepwise with water in 10% increments over 20 minutes to a final concentration of 60% cell media to 40% water (174 mOsm). 100 μl of the diluted cell/media mixture was then transferred to 8-well live cell

imaging plates (Ibidi, Cat. No. 80827), mixed with water (hypotonic condition, 87mOsm, to completely dissolve condensates) or sorbitol (Fisher Scientific, Cat. No. BP439-500) (hypertonic condition, 376 mOsm, final sorbitol concentration 250 mM) and allowed to equilibrate for 30 minutes. In some experiments, sorbitol was added to achieve varying concentrations. Osmolality was measured using a vapor pressure osmometer (Vapro 5520, Wescor). Cells were imaged using an Olympus CKX53 inverted fluorescence microscope with excitation between 488 nm and 510 nm using the 40X objective and representative images were captured. The GFP channel was isolated and converted to inverted grayscale images in Fiji. For puncta counting experiments, the fraction (percentage) of cells with condensates was quantified by counting the number of cells with condensates and dividing by total number of cells at varying osmolalities. Movies of transfected S2 cells were acquired with a Leica SP8 with 405, 488, 561, and 633 nm laser lines, using a HC PL APO CS2 63x, 1.4 numerical aperture oil objective with a 1x zoom factor. Images were acquired in an 8-bit 1024×1024 resolution format with 1 frame average and 2 line averages while scanning at 200 Hz.

Immunofluorescence confocal microscopy in fixed cells—Cells were plated on Biocoat coverslips and allowed to adhere overnight. Hypertonic stress media and fixative (4% paraformaldehyde in hypertonic stress media) solutions were warmed to 37° C. Media was aspirated off and hypertonic stress media was applied to cells. Cells were incubated in stress media in a 37°C CO_2 incubator for 5 minutes. The stress media was aspirated and warmed hypertonic fixative was applied to cells for 15 minutes at 37° C. Following fixation, the paraformaldehyde was quenched with 50mM NH4Cl, and the cells were permeabilized with 0.1% Triton X-100. Following washing with PBS w/ Ca^{2+} and Mg^{2+} ($PBS^{+/+}$) the cells were incubated for 1h at room temperature with blocking solution containing FBS and fish gelatin (1% w/vol). Primary antibody was diluted in block solution and applied overnight at 4°C. The next day, following washes with block solution, fluorescent secondary antibodies (diluted in block solution) were applied in the dark for 2h at room temperature. Following additional washes in block solution, cells were stained with a To-Pro3 in block solution (diluted 1:5000; Invitrogen, T3605) at room temperature for 20 minutes. After a final set of washes, coverslips were mounted onto slides using ProLong Glass (Invitrogen, P36980).

For standard confocal microscopy, images were acquired with a Leica TCS SP5 CW-STED with 488, 552, and 633 nm laser lines, using a HCX PL APO CS 40x, 1.25 numerical aperture oil objective with a 4x zoom factor. Images were acquired in a 12-bit 1024×1024 resolution format with 4 frame averages and 8 line averages. Crosstalk between channels was mitigated with sequential channel scanning. Confocal images with high-resolution adaptive deconvolution processing were obtained with a Leica Stellaris 8 FALCON FLIM white light laser scanning confocal microscope, using a Leica HC Pl APO CS2 63X, 1.40 numerical aperture oil objective with a 3x zoom factor. mNeonGreen and mRuby2-specific spectra were imported to LAS-X from FPBase. Scan speed was set to 400Hz and images were captured in a 2048×2048 resolution 16-bit format with 4 line averages. Confocal images were processed adaptively using Lightning deconvolution software (Leica). Sequential scanning was used to prevent channel crosstalk. In all cases, multiple confocal

fields were obtained from at least two biological replicates, obtained over the course of 2–3 independent experiments.

CLEM—HEK293 cells were grown in 6-well dishes and transfected with full-length mRuby2-WNK1. 24h post-transfection, cells were re-plated onto poly-D-lysine-coated MatTek dishes and allowed to grow for an additional 24h. Growth media was then replaced with complete media supplemented with 500mM sorbitol (hypertonic). All cells were incubated in a 37-degree CO_2 incubator for 3 minutes before applying fixative (4% paraformaldehyde in isotonic or hypertonic media, respectively) at 37°C for 1h. Fixed cells were washed twice with PBS at room temperature without agitation and stored in PBS at 4°C until imaged.

Fluorescent images were taken on a Nikon A1 confocal microscope. Samples were first imaged with a 0.50NA 10x objective using the "ND Acquisition + Large Images" addon to create a stitched montage of images of the entire coverslip, exciting with a 561nm laser and collecting through a 595/50 filter. Regions of interest were reimaged with a 1.40NA 60x objective using Nyquist sampling (0.21μm/px) and a 3×3 stitched large image in a 20μm z-stack with 0.17μm steps. A straight scratch through the sample made with a pipette tip was used as a fiduciary mark for later alignment with the SEM data.

Following high-resolution confocal field-of-view imaging, the samples underwent post-fixation and en bloc heavy metal staining to prepare for the SEM backscatter imaging. The samples were first placed in a 1% OsO4 solution for 20 minutes, followed by three 5-minute PBS washes. Next, the samples were then placed in a 1% Tannic Acid solution for 10 minutes, followed by three 5-minute ddH_2O washes. Finally, the samples were then placed in a second 1% OsO4 solution for 15 minutes followed by three 5-minute ddH_2O washes. Samples were then stained en bloc with aqueous 2% uranyl acetate for two hours at room temperature followed by three 5-minute ddH_2O washes. The final en bloc stain used was a lead aspartate solution placed on the samples and incubated at 60°C for one hour followed by three 5-minute ddH_2O washes. After post-fixation and en bloc staining, the samples were be dehydrated and embedded in resin. Samples were dehydrated with a graded series of ethanol; 30%, 50%, 70%, 90%, 100%, followed by infiltration with four 1-hour changes of EPON embedding resin (Franks et al., 2017). Pre-formed resin blocks that fit the SEM stage are pressed into the unpolymerized resin of the samples and allowed to polymerize at 37°C for 24 hours and then 65°C for 48 hours. Once the samples were acclimated to room temperature, the coverslip from the MatTek cell dish was removed with a freeze/thaw method, alternating the dish briefly sitting in liquid N_2 and 100°C H_2O until the glass coverslip was removable.

The sample block was then transferred to the SEM holder and polished with a JEOL Handy Lap with a ThorLabs 0.3μm Calcined Alumina Lapping Sheet. Roughly 20 strokes of the Handy Lap were adequate to remove the outer membrane of the embedded cells. The sample was then coated in carbon and placed in the JEOL JSM-7800 SEM equipped with a backscatter detector for imaging. Samples were SEM imaged at 7kV. A 250x montage of the entire face of the block was taken in order to align with the 10x fluorescent image montage. The polishing, carbon coating, and 250x SEM imaging was repeated until fiduciary marks

could be identified and the precise location on both the SEM and fluorescent data could be established and correlated. Once the areas where the 60x confocal fluorescent images were taken and identified, SEM montage of the regions of interest were taken at 10Kx or 15Kx. Polishing, carbon-coating, and 10Kx or 15Kx SEM montage imaging was also repeated until cellular level fiduciary marks could be identified within the Z-planes of the fluorescent images and aligned. The high magnification SEM montages were stitched using Nikon Elements software and the Fluorescent and EM data were aligned.

FRAP—Fluorescence recovery after photobleaching (FRAP) studies were performed during live confocal fluorescence microscopy as previously reported (Boyd-Shiwarski et al., 2018) using the imaging system described above. Images were acquired with 100X objective (Nikon CFI Plan Apo TIRF Lambda, 1.49 NA) every 300 ms for 1 min. FRAP was performed using an Andor FRAPPA unit with the 488 nm laser at 100% power, 100 μs dwell time and two repeats for each spot. Image series were imported into FIJI ImageJ for analysis. To calculate the percent recovery after photobleaching we normalized the bleached region to a control non-bleached region over time. The initial fluorescence intensity of the condensate prior to photobleaching was averaged and used to normalize the data. To isolate the recovery of the mobile fraction, the minimum fluorescence intensity for each region was subtracted from the normalized fluorescence intensity over time, and normalized to constrain the prebleach signal intensity to 100% and the post bleach intensity to 0%. Data was plotted as percent recovery vs. time in seconds using Prism 9 (GraphPad).

Optogenetic screen for phase separating WNK1 domains—All optogenetic live-cell imaging experiments were performed on a Nikon A1 laser-scanning confocal microscope system outfitted with a Tokai HIT stagetop incubator utilizing 40X and/or 60X oil immersion objectives (CFI Plan Apo Lambda 60X Oil, Nikon). Following transfections and/or treatments, medium was changed to phenol red-free growth medium (GIBCO) and cells were allowed to equilibrate on the preheated (37°C and 5% CO2) stagetop incubator for 10 min prior to imaging. Acute blue light stimulation was achieved by utilizing the 488nm laser line and the stimulation module within Nikon Elements imaging software. Activation duration was set to 1s and laser power was set at 20%. Stimulation regions of interest (ROIs) were drawn over fields of view prior to image acquisition. Following 2–5 baseline images, laser stimulation was performed and cells were imaged for up to 10 min post-activation. Timing and order of image acquisition was alternated across experiments between experimental groups. Data presented are representative of at least two independent experiments utilizing three or more biological replicates per experiment.

In-cell phase diagrams—Cells were transiently transfected with mRb2-tagged WNK1 constructs. 24h later, the cells were re-plated on poly-D-lysine coated MatTek dishes. The following day (~48h post transfection), media was replaced with 1mL pre-warmed Leibovitz L-15 media. Dishes were mounted into an environmental stage set to 38°C on an inverted Leica SP8 confocal microscope with a HC PL APO CS2 63X, 1.40 numerical aperture oil objective. 6×6 tile scans were obtained every 60 seconds for 10 minutes. The scan speed was set to 700 Hz with resonant scanning deactivated, and images were acquired in a 2048×2048 resolution format. Fixed laser power for the 552 nm laser line was set

using the 1-494 mRuby2 tagged WNK1 construct as this was the most highly expressed construct, and thus the brightest. This was done to minimize oversaturation in each set of transfected cells. Stress media was added after a pre-stress tile scan was completed to obtain baseline fluorescence intensities. The stresses were composed of Leibovitz media with varying amounts of sorbitol, ranging from 50 mM (350mOsm) to 250 mM (550mOsm).

In each of the tile images, mRuby2-fluorescent cells that were clearly captured within the field of view for the duration of the stress time course were identified, assigned an identification number for blinded evaluation (Fig S4A), and pre-stress intensities were measured in FIJI. The blinded image sets were categorized by stress condition and transfected WNK1 construct but were deidentified via a randomized coding system prior to passing them on to three independent screeners. The screeners scored the degree of phase separation (no phase separation, nucleation, and spinodal decomposition) for each numbered cell. Score discrepancies were re-evaluated by the screeners as a group on a case-by-case basis to arrive at consensus. Following unblinding, data points were plotted on a graph with protein concentration on the X-axis, and osmolality on the Y-axis to compose phase diagrams. Binodal phase boundaries were drawn at the level of pre-stress fluorescence intensity where the WNK1 constructs uniformly adopted a nucleated morphology following exposure to osmotic stress, and spinodal phase boundaries were drawn in similar fashion for constructs that underwent post-stress spinodal decomposition.

Preparation of cell and tissue lysates and immunoblot analysis—To examine the natively expressed WNK-SPAK/OSR1 pathway under hyperosmotic stress, unedited HEK-293 cells or endogenous mNG-tagged WNK1 cells were grown in 6-well dishes. Once cells reached 90% confluence (~24h), growth media (complete) was replaced with fresh complete media supplemented with various amounts of sorbitol. Following the application of isotonic or stress media, cells were incubated in a 37-degree CO_2 incubator for 5 minutes, and then harvested (~5 minutes) in the same applied isotonic or stress media. Collected samples were immediately pelleted at 4°C for 5 minutes and the supernatant discarded, totaling 15 minutes of exposure to osmotic stress. For experiments with transfected WNK1 constructs, WNK1/WNK3 DKO cells were grown in 6-well plates and transfected, in duplicate, with varying amounts (0.5–3.5ng) of one of the following mRuby2-tagged WNK1 constructs: full-length,1-494 fragment, 1-1242 fragment, or the double coiled-coil mutant. Based on pilot studies, transfection amounts were adjusted to minimize differences in protein expression among each of the constructs. 24h post-transfection, cells were re-plated, dividing each well of transfected cells in two. After an additional 24h, growth media (complete) from one divided well was replaced with fresh complete media (iso), and growth media from the second divided well replaced with complete media supplemented with 50mM sorbitol (hyper). Cells were placed in a 37-degree CO_2 incubator for 20 minutes and then harvested in the same applied media (~5 minutes). Collected samples were immediately pelleted at 4°C for 5 minutes and the supernatant discarded, totaling 30 minutes of exposure to osmotic stress. All other unedited cells and candidate clones were washed with chilled DPBS and collected in chilled PBS supplemented with protease (Thermo Fisher Scientific) and phosphatase (Roche) inhibitor cocktails. Collected samples were immediately pelleted at 4°C for 5 minutes.

Cytosolic proteins were extracted from cell pellets with ice-cold Detergent Lysis Buffer (50mM Tris-Hcl pH 8.0, 1% IGEPAL CA 630, 0.4% sodium deoxycholate, 62.5mM EDTA, supplemented with protease and phosphatase inhibitors). Lysates were incubated on ice for 20 minutes before pelleting out insoluble materials via hard centrifugation at 4°C for 10 minutes. Supernatant protein concentrations were determined using the Pierce BCA Protein Assay Kit (Thermo Fisher Scientific). Equal amounts of protein (20ug) were denatured in Laemmli buffer, maintained at room temperature for 10 minutes, and loaded onto 4–20% Criterion TGX precast gels (Bio-Rad) alongside Precision Plus All Blue Standard (Bio-Rad) for SDS-PAGE. Once separated, the proteins were transferred to a nitrocellulose membrane using Bio-Rad Trans-Blot Turbo for immunoblotting. The resulting signal was visualized with enhanced chemiluminescence and measured using a Bio-Rad ChemiDoc imager.

For immunoblotting data obtained in transfected osmotically stressed cells, gel lanes represent individual biological replicates, and are representative of data obtained over three to five independent experiments, which were used for quantification and statistical analysis.

For protein isolation from tissue, whole kidney and brain cortex was homogenized in ice-cold RIPA extraction buffer (Thermo Scientific) with freshly added protease and phosphatase inhibitors. Following agitation at 4°C for 30min, homogenates were centrifuged and supernatants were collected. Equal amounts of protein, as determined by BCA protein assay, were fractionated by SDS-PAGE on 4–15% Criterion TGX precast gels, transferred to nitrocellulose, and immunoblotted with NKCC1 antibody, as described above. ECL signal was visualized by autoradiography.

Cell volume measurements—HEK-293 WNK1/WNK3 DKO cells were plated in 6-well dishes in complete media and allowed to grow to 80–90% confluency. Cells were transfected in antibiotic-free media the following day with standardized amounts of mRuby2 tagged WNK1 plasmids and pEGFP-N1. Since eGFP distributes uniformly throughout the nucleus and cytoplasm, it was used as a fluorescent marker for transfected cell volume. Cells were re-plated 24h post-transfection on poly-D-lysine coated MatTek dishes. Tonic solutions and media were prepared and warmed to 37°C on the day of imaging. Cell media was replaced with Leibovitz L-15 media supplemented with 10 μM Cariporide, with or without 20 μM Bumetanide. Both cariporide and bumetanide were solubilized in DMSO; the addition of these inhibitors increased osmolality by 7 and 13mOsm, respectively. Following a 10 min preincubation period, the plated cells were imaged with a Leica SP8 live cell resonant scanning confocal microscope on a climate-controlled stage set to 38°C. Confocal stacks (20–30 steps, 2μm step size) capturing whole-cell eGFP signal were taken with a Leica 40x, 1.1 numerical aperture water immersion objective every 30 seconds for 20 minutes at a scan speed of 8000Hz. For each experimental condition, a control set of calibration measurements was taken to account for natural drift in cell volume in Leibowitz media on the heated stage over a 20-minute time course. To evaluate volume changes after hypertonic stress, following the first 60 seconds of imaging, sorbitol was added to achieve a final concentration of 50mM, which increased solution osmolality by 50mOsm. Confocal stacks were rendered in the LasX 3D software platform. Uncommonly, field boundaries were cropped during post-processing to exclude floating cells that would confound volume calculations. Following background subtraction, Otsu thresholding was applied to obtain

binary images. The integrated binary whole-cell GFP signal from each confocal stack was used to calculate the percent cell volume per imaging field; this reliably reflected volumetric changes over the time course.

For cell volume calculations, percent volume per field measurements were normalized to 100% at time zero. Changes in cell volume over time were adjusted by the control set of drift calibration measurements. RVI was defined as the percent volume recovery during the time course following exposure to hypertonic stress. To account for variability in baseline volume reduction after hypertonic exposure, this percentage was expressed relative to the volume lost, using the following equation:

$$Percent\ volume\ recovered\ (RVI) = \left[\frac{\left(\frac{V_t}{V_{min}}\right) - 1}{(V_0 - V_{min})}\right] \times 100$$

Where V_0 = the volume at time zero (normalized to 1), V_{min} = the minimal fractional cell volume measured immediately following exposure to hypertonicity, and V_t = the fractional cell volume at a given time point during the RVI phase.

Rubidium influx assay—WNK1/3 DKO cells expressing full-length or 1-494 WNK1 were cultured in PDL coated 24-well plates with DMEM culture media until 90% confluent. The culture medium was removed and cells were rinsed with an isotonic buffer (310 mOsm, containing 134 mM NaCl, 2 mM $CaCl_2$, 0.8 mM NaH_2PO_4, 5 mM glucose, 25 mM HEPES and 1.66 mM $MgSO_4$) as described before (Luo et al., 2020). To measure basal K^+ (Rb^+) influx, cells were exposed to the isotonic buffer (310 mOsm, pH 7.4, containing 5.36 mM Rb^+,) in the absence or presence of NKCC1 inhibitor bumetanide (BMT, 10 μM), for 10 min at 37°C. To measure changes of Rb^+ influx in HEK293 cells in response to hypertonic stress, cells were exposed to the hypertonic solution (370 mOsm adjusted by adding 60 mM sucrose, pH 7.4, 5.36 mM Rb^+) for 5 min at 37°C. To terminate Rb^+ influx, cells were washed with the isotonic or hypertonic washing solutions (Rb^+ free) and lysed with 200 mL 0.15% SDS (room temperature) to release the intracellular Rb^+. The intracellular Rb^+ concentration in cell lysates was measured using an automated atomic absorption spectrophotometer (Ion Channel Reader, ICR-8000; Aurora Biomed, Vancouver, Canada). Total protein of cell lysates was measured by BCA assay. Rb^+ influx rate was calculated and expressed as mg Rb^+/mg protein/min. NKCC1-mediated Rb^+ influx was determined by subtracting Rb^+ influx value in the presence of bumetanide from the total Rb^+ influx. To calculate shrinkage-induced bumetanide-sensitive Rb+ flux, we subtracted the baseline bumetanide-sensitive Rb+ transport measured under isotonic conditions (310mOsm), from the increase in bumetanide-sensitive Rb+ transport measured under hypertonic conditions (370mOsm).

Crowding agent microinjection studies—Borosilicate glass filaments (O.D. 1.2 mm, I.D. 0.94 mm, 10cm length, Catalog #: BF120-94-10 Sutter Instrument) were pulled into micropipettes using a Sutter Instrument P-1000. A potassium acetate HEPES buffer (KH buffer, 125 mM K+ Acetate, 25 mM HEPES, pH 7.4), was prepared as the vehicle for

microinjection and 1.5 μL was backfilled into the pulled micropipettes (Shiwarski et al., 2017). For isosmotic injections, stock KH buffer was injected into mNG-WNK1 cells using an Eppendorf FemtoJet (pi = 35 hPa, ti(s) = 0.2, pc(hPa) = 20) and InjectMan micromanipulators on a Nikon Ti-E-2000. Widefield fluorescence imaging and brightfield DIC was performed using a 100X objective (Nikon CFI Plan Apo TIRF Lambda, 1.49 NA), a GFP excitation/emission filter cube (Nikon), a stage top incubator (TokaiHIT), and a Prime 95B camera (Photometrics) run with Micro-Manager software (Edelstein et al., 2014). Time-lapse imaging (300 ms exposure, 30 s interval, for 15 min) was performed at 37°C prior to and during injection. A hyperosmotic solution was prepared by adding KCl (100 mM) 1:1 to the KH buffer to yield a 50 mM final concentration. To induce molecular crowding, a Ficoll solution (50% w/v Ficoll PM400, GE Healthcare, in 50 mM HEPES pH 7.4) was combined 1:1 with the KH buffer and microinjected into the cells as described for the isosmotic condition. In experiments injecting multiple solutions into the same cells, micropipettes were preloaded prior to the experiment and exchanged between treatments. Image analysis was performed using FIJI.

Cell size measurements—Isotonic cell size measurements were carried out with an Amnis ImageStream flow cytometer (Luminex), based on previously published methods (Samsel et al., 2013). mRuby2-tagged full length WNK1 and WNK1-1-494 were transiently transfected in HEK-293 cells. Transfected cells were harvested in Leibovitz L-15 media (Gibco) 48h post transfection. Before analyzing the transfected cells, the cells were further diluted with FACS buffer. mRuby2 fluorescence signal was detected by using a filter with wavelength 642–745nm. At least 8000 images were collected per transfection replicate. From each transfection replicate, around 10–15000 events meeting the cell classifier were acquired. Each replicate acquisition file was analyzed using IDEAS 5.0 software (Amnis corporation, Seattle, WA). A hierarchical gating strategy was used to identify single cells. Doublets were eliminated by gating on single cells using intensity versus aspect ratio brightfield plot. Single cells have higher aspect ratio as compared to the doublets or aggregates. The mean area or size of single cells was determined in microns (μm) by using IDEAS software.

Bioinformatic analysis—We used three algorithms to predict WNK protein disorder: SPOT-Disorder (Hanson et al., 2017), VSL2B (Obradovic et al., 2005), and VL3H (Peng et al., 2005). SEG was used to predict low complexity regions (LCRs) (Wootton, 1994). Short, medium, and long low-complexity segments were defined as having trigger window length (W), trigger complexity ($K_2(1)$) and extension complexity ($K_2(2)$) parameters of 12/2.2/2.5, 25/3.0/3.3, and 45/3.4/3.75, respectively. NCoils (Lupas et al., 1991) with a sliding window of 21 or 28 residues was used to predict coiled-coil domains. Marcoil (Delorenzi and Speed, 2002) was used to predict CC heptad registers in rat WNK1. Prion-like domains (PLDs) were predicted using PLAAC (Lancaster et al., 2014). A default core length of 60 and a relative alpha of 50% was used. Similar results were obtained when the relative background frequency alpha for *S. cerevesiae* was adjusted to 0% (i.e., 100% for the species being scored: human, rat, *Drosophila*, or *C. elegans*).

Details on the protein sequences used to analyze cross-species amino acid compositional bias in WNK CTDs are provided in the Mendeley dataset. In most cases, UniprotKb was used to identify specific WNK kinases. Once the sequence for a putative WNK kinase was found, we confirmed its identity by verifying that the kinase domain contained the atypically placed catalytic lysine (Min et al., 2004) and chloride binding pocket that are defining features of the WNKs (Piala et al., 2014). The CTD was defined as the sequence downstream from the predicted PF2-like domain. Amino acid frequencies within the CTD were stratified using the Expasy ProtParam tool.

QUANTIFICATION AND STATISTICAL ANALYSIS

Statistical details of experiments, including n, P-values, and specifics regarding post-hoc testing can be found in the figures, figure legends, and methods. Statistical analysis was performed using GraphPad Prism software and are presented as mean ± SEM. Comparisons between two groups were determined by Student's t-test. Multiple comparisons were determined by one- or two-way ANOVA followed by post-hoc testing as indicated in the figure legends. RVI time series data were analyzed by repeated measures two-way ANOVA, followed by Sidak's post test. Significance criterion was set at a P-value of ≤0.05. For colocalization studies in fixed cells, percent colocalization was determined by thresholded Mander's Overlap Coefficients, using the JaCOP plugin in FIJI.

Supplementary Material

Refer to Web version on PubMed Central for supplementary material.

Acknowledgments

This work was supported by National Institutes of Health grants K08DK118211 (C.B-S.); K99HL155777 (D.J.S.); R01DK098145 and R01DK119252 (A.R.S.); P30DK79307, S10OD021627, and S10OD028596 (Pittsburgh Center for Kidney Research); R01DK110358 (A.R.R.); and U.S Department of Veterans Affairs grants I01BX002891 and IK6BX005647 (D.S.).

We thank Ora Weisz, Catherine Baty, Gerard Apodaca, Manoj Puthenveedu, and Donna Stolz for imaging support, Gabrielle Pittman for technical assistance, and Ossama Kashlan, Seth Childers, Jeff Brodsky, Helbert Rondon, and Todd Lamitina for helpful discussions. This content is solely the responsibility of the authors and does not necessarily represent the official views of the U.S. Department of Veterans Affairs.

References

Acevedo SF, Peru y Colon de Portugal RL, Gonzalez DA, Rodan AR, and Rothenfluh A (2015). S6 Kinase Reflects and Regulates Ethanol-Induced Sedation. J Neurosci 35, 15396–15402. [PubMed: 26586826]

Akella R, Humphreys JM, Sekulski K, He H, Durbacz M, Chakravarthy S, Liwocha J, Mohammed ZJ, Brautigam CA, and Goldsmith EJ (2021). Osmosensing by WNK Kinases. Mol Biol Cell 32, 1614–1623. [PubMed: 33689398]

Alberti S, Gladfelter A, and Mittag T (2019). Considerations and Challenges in Studying Liquid-Liquid Phase Separation and Biomolecular Condensates. Cell 176, 419–434. [PubMed: 30682370]

Andre AAM, and Spruijt E (2020). Liquid-Liquid Phase Separation in Crowded Environments. Int J Mol Sci 21.

Bhuiyan MI, Song S, Yuan H, Begum G, Kofler J, Kahle KT, Yang SS, Lin SH, Alper SL, Subramanya AR, et al. (2016). WNK-Cab39-NKCC1 signaling increases the susceptibility to ischemic brain damage in hypertensive rats. J Cereb Blood Flow Metab.

Boyd-Shiwarski CR, Shiwarski DJ, Roy A, Namboodiri HN, Nkashama LJ, Xie J, McClain KL, Marciszyn A, Kleyman TR, Tan RJ, et al. (2018). Potassium-regulated distal tubule WNK bodies are kidney-specific WNK1 dependent. Mol Biol Cell 29, 499–509. [PubMed: 29237822]

Burg MB (1995). Molecular basis of osmotic regulation. Am J Physiol 268, F983–996. [PubMed: 7611465]

Carmosino M, Gimenez I, Caplan M, and Forbush B (2008). Exon loss accounts for differential sorting of Na-K-Cl cotransporters in polarized epithelial cells. Mol Biol Cell 19, 4341–4351. [PubMed: 18667527]

Colclasure GC, and Parker JC (1991). Cytosolic protein concentration is the primary volume signal in dog red cells. J Gen Physiol 98, 881–892. [PubMed: 1662684]

Daigle JG, Krishnamurthy K, Ramesh N, Casci I, Monaghan J, McAvoy K, Godfrey EW, Daniel DC, Johnson EM, Monahan Z, et al. (2016). Pur-alpha regulates cytoplasmic stress granule dynamics and ameliorates FUS toxicity. Acta Neuropathol 131, 605–620. [PubMed: 26728149]

de Los Heros P, Pacheco-Alvarez D, and Gamba G (2018). Role of WNK Kinases in the Modulation of Cell Volume. Curr Top Membr 81, 207–235. [PubMed: 30243433]

Delarue M, Brittingham GP, Pfeffer S, Surovtsev IV, Pinglay S, Kennedy KJ, Schaffer M, Gutierrez JI, Sang D, Poterewicz G, et al. (2018). mTORC1 Controls Phase Separation and the Biophysical Properties of the Cytoplasm by Tuning Crowding. Cell 174, 338–349 e320. [PubMed: 29937223]

Delorenzi M, and Speed T (2002). An HMM model for coiled-coil domains and a comparison with PSSM-based predictions. Bioinformatics 18, 617–625. [PubMed: 12016059]

Delpire E, and Gagnon KB (2018). Water Homeostasis and Cell Volume Maintenance and Regulation. Curr Top Membr 81, 3–52. [PubMed: 30243436]

Demian WL, Persaud A, Jiang C, Coyaud E, Liu S, Kapus A, Kafri R, Raught B, and Rotin D (2019). The Ion Transporter NKCC1 Links Cell Volume to Cell Mass Regulation by Suppressing mTORC1. Cell reports 27, 1886–1896 e1886. [PubMed: 31067471]

Edelstein AD, Tsuchida MA, Amodaj N, Pinkard H, Vale RD, and Stuurman N (2014). Advanced methods of microscope control using muManager software. J Biol Methods 1.

Fiumara F, Fioriti L, Kandel ER, and Hendrickson WA (2010). Essential role of coiled coils for aggregation and activity of Q/N-rich prions and PolyQ proteins. Cell 143, 1121–1135. [PubMed: 21183075]

Flagella M, Clarke LL, Miller ML, Erway LC, Giannella RA, Andringa A, Gawenis LR, Kramer J, Duffy JJ, Doetschman T, et al. (1999). Mice lacking the basolateral Na-K-2Cl cotransporter have impaired epithelial chloride secretion and are profoundly deaf. J Biol Chem 274, 26946–26955. [PubMed: 10480906]

Flemmer AW, Gimenez I, Dowd BF, Darman RB, and Forbush B (2002). Activation of the Na-K-Cl cotransporter NKCC1 detected with a phospho-specific antibody. J Biol Chem 277, 37551–37558. [PubMed: 12145305]

Ford LK, and Fioriti L (2020). Coiled-Coil Motifs of RNA-Binding Proteins: Dynamicity in RNA Regulation. Front Cell Dev Biol 8, 607947. [PubMed: 33330512]

Franks J, Wallace CT, Shibata M, Suga M, Erdman N, Stolz DB, and Watkins SC (2017). Correlative Fluorescence and Electron Microscopy in 3D-Scanning Electron Microscope Perspective. Curr Protoc Cytom 80, 12 45 11–12 45 15.

Franzmann TM, Jahnel M, Pozniakovsky A, Mahamid J, Holehouse AS, Nuske E, Richter D, Baumeister W, Grill SW, Pappu RV, et al. (2018). Phase separation of a yeast prion protein promotes cellular fitness. Science 359.

Garner MM, and Burg MB (1994). Macromolecular crowding and confinement in cells exposed to hypertonicity. Am J Physiol 266, C877–892. [PubMed: 8178962]

Gimenez I, and Forbush B (2003). Short-term stimulation of the renal Na-K-Cl cotransporter (NKCC2) by vasopressin involves phosphorylation and membrane translocation of the protein. J Biol Chem 278, 26946–26951. [PubMed: 12732642]

Gonzalez M, Martin-Ruiz I, Jimenez S, Pirone L, Barrio R, and Sutherland JD (2011). Generation of stable Drosophila cell lines using multicistronic vectors. Sci Rep 1, 75. [PubMed: 22355594]

Hansen SH, Sandvig K, and van Deurs B (1993). Clathrin and HA2 adaptors: effects of potassium depletion, hypertonic medium, and cytosol acidification. J Cell Biol 121, 61–72. [PubMed: 8458873]

Hanson J, Yang Y, Paliwal K, and Zhou Y (2017). Improving protein disorder prediction by deep bidirectional long short-term memory recurrent neural networks. Bioinformatics 33, 685–692. [PubMed: 28011771]

He G, Wang HR, Huang SK, and Huang CL (2007). Intersectin links WNK kinases to endocytosis of ROMK1. J Clin Invest 117, 1078–1087. [PubMed: 17380208]

Heuser JE, and Anderson RG (1989). Hypertonic media inhibit receptor-mediated endocytosis by blocking clathrin-coated pit formation. J Cell Biol 108, 389–400. [PubMed: 2563728]

Hoffmann EK, Lambert IH, and Pedersen SF (2009). Physiology of cell volume regulation in vertebrates. Physiol Rev 89, 193–277. [PubMed: 19126758]

Hyman AA, Weber CA, and Julicher F (2014). Liquid-liquid phase separation in biology. Annu Rev Cell Dev Biol 30, 39–58. [PubMed: 25288112]

Jalihal AP, Pitchiaya S, Xiao L, Bawa P, Jiang X, Bedi K, Parolia A, Cieslik M, Ljungman M, Chinnaiyan AM, et al. (2020). Multivalent Proteins Rapidly and Reversibly Phase-Separate upon Osmotic Cell Volume Change. Mol Cell 79, 978–990 e975. [PubMed: 32857953]

Lancaster AK, Nutter-Upham A, Lindquist S, and King OD (2014). PLAAC: a web and command-line application to identify proteins with prion-like amino acid composition. Bioinformatics 30, 2501–2502. [PubMed: 24825614]

Lee DH, Maunsbach AB, Riquier-Brison AD, Nguyen MT, Fenton RA, Bachmann S, Yu AS, and McDonough AA (2013). Effects of ACE inhibition and ANG II stimulation on renal Na-Cl cotransporter distribution, phosphorylation, and membrane complex properties. Am J Physiol Cell Physiol 304, C147–163. [PubMed: 23114965]

Leslie M (2021). Separation anxiety. Science 371, 336–338. [PubMed: 33479134]

Li P, Banjade S, Cheng HC, Kim S, Chen B, Guo L, Llaguno M, Hollingsworth JV, King DS, Banani SF, et al. (2012). Phase transitions in the assembly of multivalent signalling proteins. Nature 483, 336–340. [PubMed: 22398450]

Li Y, Hu J, Vita R, Sun B, Tabata H, and Altman A (2004). SPAK kinase is a substrate and target of PKCtheta in T-cell receptor-induced AP-1 activation pathway. EMBO J 23, 1112–1122. [PubMed: 14988727]

Liu Z, Demian W, Persaud A, Jiang C, Subramanaya AR, and Rotin D (2022). Regulation of the p38-MAPK pathway by hyperosmolarity and by WNK kinases. Sci Rep 12, 14480. [PubMed: 36008477]

Luo L, Wang J, Ding D, Hasan MN, Yang SS, Lin SH, Schreppel P, Sun B, Yin Y, Erker T, et al. (2020). Role of NKCC1 Activity in Glioma K(+) Homeostasis and Cell Growth: New Insights With the Bumetanide-Derivative STS66. Front Physiol 11, 911. [PubMed: 32848856]

Lupas A, Van Dyke M, and Stock J (1991). Predicting coiled coils from protein sequences. Science 252, 1162–1164. [PubMed: 2031185]

Mann JR, Gleixner AM, Mauna JC, Gomes E, DeChellis-Marks MR, Needham PG, Copley KE, Hurtle B, Portz B, Pyles NJ, et al. (2019). RNA Binding Antagonizes Neurotoxic Phase Transitions of TDP-43. Neuron 102, 321–338 e328. [PubMed: 30826182]

McSwiggen DT, Mir M, Darzacq X, and Tjian R (2019). Evaluating phase separation in live cells: diagnosis, caveats, and functional consequences. Genes Dev 33, 1619–1634. [PubMed: 31594803]

Min X, Lee BH, Cobb MH, and Goldsmith EJ (2004). Crystal structure of the kinase domain of WNK1, a kinase that causes a hereditary form of hypertension. Structure 12, 1303–1311. [PubMed: 15242606]

Minton AP, Colclasure GC, and Parker JC (1992). Model for the role of macromolecular crowding in regulation of cellular volume. Proc Natl Acad Sci U S A 89, 10504–10506. [PubMed: 1332050]

Nickerson AJ, and Rajendran VM (2021). Aldosterone up-regulates basolateral Na(+) -K(+) −2Cl(−) cotransporter-1 to support enhanced large-conductance K(+) channel-mediated K(+) secretion in rat distal colon. FASEB J 35, e21606. [PubMed: 33908679]

Nott TJ, Petsalaki E, Farber P, Jervis D, Fussner E, Plochowietz A, Craggs TD, Bazett-Jones DP, Pawson T, Forman-Kay JD, et al. (2015). Phase transition of a disordered nuage protein

generates environmentally responsive membraneless organelles. Mol Cell 57, 936–947. [PubMed: 25747659]

O'Neill WC (1999). Physiological significance of volume-regulatory transporters. Am J Physiol 276, C995–C1011. [PubMed: 10329946]

Obradovic Z, Peng K, Vucetic S, Radivojac P, and Dunker AK (2005). Exploiting heterogeneous sequence properties improves prediction of protein disorder. Proteins 61 Suppl 7, 176–182.

Orlov SN, Shiyan A, Boudreault F, Ponomarchuk O, and Grygorczyk R (2018). Search for Upstream Cell Volume Sensors: The Role of Plasma Membrane and Cytoplasmic Hydrogel. Curr Top Membr 81, 53–82. [PubMed: 30243440]

Pacheco-Alvarez D, Carrillo-Perez DL, Mercado A, Leyva-Rios K, Moreno E, Hernandez-Mercado E, Castaneda-Bueno M, Vazquez N, and Gamba G (2020). WNK3 and WNK4 exhibit opposite sensitivity with respect to cell volume and intracellular chloride concentration. Am J Physiol Cell Physiol 319, C371–C380. [PubMed: 32579473]

Parker JC (1993). In defense of cell volume? Am J Physiol 265, C1191–1200. [PubMed: 8238472]

Parker JC, and Colclasure GC (1992). Macromolecular crowding and volume perception in dog red cells. Mol Cell Biochem 114, 9–11. [PubMed: 1334230]

Peng K, Vucetic S, Radivojac P, Brown CJ, Dunker AK, and Obradovic Z (2005). Optimizing long intrinsic disorder predictors with protein evolutionary information. J Bioinform Comput Biol 3, 35–60. [PubMed: 15751111]

Pereira EM, Labilloy A, Eshbach ML, Roy A, Subramanya AR, Monte S, Labilloy G, and Weisz OA (2016). Characterization and phosphoproteomic analysis of a human immortalized podocyte model of Fabry disease generated using CRISPR/Cas9 technology. Am J Physiol Renal Physiol 311, F1015–F1024. [PubMed: 27681560]

Piala AT, Moon TM, Akella R, He H, Cobb MH, and Goldsmith EJ (2014). Chloride sensing by WNK1 involves inhibition of autophosphorylation. Sci Signal 7, ra41. [PubMed: 24803536]

Pleiner T, Hazu M, Tomaleri GP, Januszyk K, Oania RS, Sweredoski MJ, Moradian A, Guna A, and Voorhees RM (2021). WNK1 is an assembly factor for the human ER membrane protein complex. Mol Cell 81, 2693–2704 e2612. [PubMed: 33964204]

Pleinis JM, Norrell L, Akella R, Humphreys JM, He H, Sun Q, Zhang F, Sosa-Pagan J, Morrison DE, Schellinger JN, et al. (2021). WNKs are potassium-sensitive kinases. Am J Physiol Cell Physiol 320, C703–C721. [PubMed: 33439774]

Portz B, Lee BL, and Shorter J (2021). FUS and TDP-43 Phases in Health and Disease. Trends Biochem Sci 46, 550–563. [PubMed: 33446423]

Ramakrishna S, Cho SW, Kim S, Song M, Gopalappa R, Kim JS, and Kim H (2014). Surrogate reporter-based enrichment of cells containing RNA-guided Cas9 nuclease-induced mutations. Nature communications 5, 3378.

Riback JA, Zhu L, Ferrolino MC, Tolbert M, Mitrea DM, Sanders DW, Wei MT, Kriwacki RW, and Brangwynne CP (2020). Composition-dependent thermodynamics of intracellular phase separation. Nature 581, 209–214. [PubMed: 32405004]

Rinehart J, Maksimova YD, Tanis JE, Stone KL, Hodson CA, Zhang J, Risinger M, Pan W, Wu D, Colangelo CM, et al. (2009). Sites of regulated phosphorylation that control K-Cl cotransporter activity. Cell 138, 525–536. [PubMed: 19665974]

Rodan AR (2018). WNK-SPAK/OSR1 signaling: lessons learned from an insect renal epithelium. Am J Physiol Renal Physiol 315, F903–F907. [PubMed: 29923766]

Roy A, Al-Qusairi L, Donnelly BF, Ronzaud C, Marciszyn AL, Gong F, Chang YP, Butterworth MB, Pastor-Soler NM, Hallows KR, et al. (2015a). Alternatively spliced proline-rich cassettes link WNK1 to aldosterone action. J Clin Invest 125, 3433–3448. [PubMed: 26241057]

Roy A, Goodman JH, Begum G, Donnelly BF, Pittman G, Weinman EJ, Sun D, and Subramanya AR (2015b). Generation of WNK1 knockout cell lines by CRISPR/Cas-mediated genome editing. Am J Physiol Renal Physiol 308, F366–376. [PubMed: 25477473]

Samsel L, Dagur PK, Raghavachari N, Seamon C, Kato GJ, and McCoy JP Jr. (2013). Imaging flow cytometry for morphologic and phenotypic characterization of rare circulating endothelial cells. Cytometry B Clin Cytom 84, 379–389. [PubMed: 23554273]

Sang D, Shu T, Pantoja CF, Ibanez de Opakua A, Zweckstetter M, and Holt LJ (2022). Condensed-phase signaling can expand kinase specificity and respond to macromolecular crowding. Mol Cell.

Serra SA, Stojakovic P, Amat R, Rubio-Moscardo F, Latorre P, Seisenbacher G, Canadell D, Bottcher R, Aregger M, Moffat J, et al. (2021). LRRC8A-containing chloride channel is crucial for cell volume recovery and survival under hypertonic conditions. Proc Natl Acad Sci U S A 118.

Shimobayashi SF, Ronceray P, Sanders DW, Haataja MP, and Brangwynne CP (2021). Nucleation landscape of biomolecular condensates. Nature.

Shin Y, Berry J, Pannucci N, Haataja MP, Toettcher JE, and Brangwynne CP (2017). Spatiotemporal Control of Intracellular Phase Transitions Using Light-Activated optoDroplets. Cell 168, 159–171 e114. [PubMed: 28041848]

Shin Y, and Brangwynne CP (2017). Liquid phase condensation in cell physiology and disease. Science 357.

Shiwarski DJ, Crilly SE, Dates A, and Puthenveedu MA (2019). Dual RXR motifs regulate nerve growth factor-mediated intracellular retention of the delta opioid receptor. Mol Biol Cell 30, 680–690. [PubMed: 30601694]

Shiwarski DJ, Darr M, Telmer CA, Bruchez MP, and Puthenveedu MA (2017). PI3K class II alpha regulates delta-opioid receptor export from the trans-Golgi network. Mol Biol Cell 28, 2202–2219. [PubMed: 28566554]

Sodek J, Hodges RS, Smillie LB, and Jurasek L (1972). Amino-acid sequence of rabbit skeletal tropomyosin and its coiled-coil structure. Proc Natl Acad Sci U S A 69, 3800–3804. [PubMed: 4509342]

Sorensen MV, Grossmann S, Roesinger M, Gresko N, Todkar AP, Barmettler G, Ziegler U, Odermatt A, Loffing-Cueni D, and Loffing J (2013). Rapid dephosphorylation of the renal sodium chloride cotransporter in response to oral potassium intake in mice. Kidney Int 83, 811–824. [PubMed: 23447069]

Steffensen AB, Oernbo EK, Stoica A, Gerkau NJ, Barbuskaite D, Tritsaris K, Rose CR, and MacAulay N (2018). Cotransporter-mediated water transport underlying cerebrospinal fluid formation. Nature communications 9, 2167.

Subramanya AR, and Ellison DH (2014). Distal convoluted tubule. Clin J Am Soc Nephrol 9, 2147–2163. [PubMed: 24855283]

Taslimi A, Vrana JD, Chen D, Borinskaya S, Mayer BJ, Kennedy MJ, and Tucker CL (2014). An optimized optogenetic clustering tool for probing protein interaction and function. Nature communications 5, 4925.

Thastrup JO, Rafiqi FH, Vitari AC, Pozo-Guisado E, Deak M, Mehellou Y, and Alessi DR (2012). SPAK/OSR1 regulate NKCC1 and WNK activity: analysis of WNK isoform interactions and activation by T-loop trans-autophosphorylation. Biochem J 441, 325–337. [PubMed: 22032326]

Walter H, and Brooks DE (1995). Phase separation in cytoplasm, due to macromolecular crowding, is the basis for microcompartmentation. FEBS Lett 361, 135–139. [PubMed: 7698310]

Wang J, Choi JM, Holehouse AS, Lee HO, Zhang X, Jahnel M, Maharana S, Lemaitre R, Pozniakovsky A, Drechsel D, et al. (2018). A Molecular Grammar Governing the Driving Forces for Phase Separation of Prion-like RNA Binding Proteins. Cell 174, 688–699 e616. [PubMed: 29961577]

Watanabe K, Morishita K, Zhou X, Shiizaki S, Uchiyama Y, Koike M, Naguro I, and Ichijo H (2021). Cells recognize osmotic stress through liquid-liquid phase separation lubricated with poly(ADP-ribose). Nature communications 12, 1353.

Wootton JC (1994). Non-globular domains in protein sequences: automated segmentation using complexity measures. Comput Chem 18, 269–285. [PubMed: 7952898]

Wu Y, Schellinger JN, Huang CL, and Rodan AR (2014). Hypotonicity stimulates potassium flux through the WNK-SPAK/OSR1 kinase cascade and the Ncc69 sodium-potassium-2-chloride cotransporter in the Drosophila renal tubule. J Biol Chem 289, 26131–26142. [PubMed: 25086033]

Xu B, English JM, Wilsbacher JL, Stippec S, Goldsmith EJ, and Cobb MH (2000). WNK1, a novel mammalian serine/threonine protein kinase lacking the catalytic lysine in subdomain II. J Biol Chem 275, 16795–16801. [PubMed: 10828064]

Zagorska A, Pozo-Guisado E, Boudeau J, Vitari AC, Rafiqi FH, Thastrup J, Deak M, Campbell DG, Morrice NA, Prescott AR, et al. (2007). Regulation of activity and localization of the WNK1 protein kinase by hyperosmotic stress. J Cell Biol 176, 89–100. [PubMed: 17190791]

Zhang J, Bhuiyan MIH, Zhang T, Karimy JK, Wu Z, Fiesler VM, Zhang J, Huang H, Hasan MN, Skrzypiec AE, et al. (2020). Modulation of brain cation-Cl(−) cotransport via the SPAK kinase inhibitor ZT-1a. Nature communications 11, 78.

Zimmerman SB, and Harrison B (1987). Macromolecular crowding increases binding of DNA polymerase to DNA: an adaptive effect. Proc Natl Acad Sci U S A 84, 1871–1875. [PubMed: 3550799]

Highlights

- Endogenous WNK1 forms hyperosmotic stress-induced condensates
- The intrinsically disordered C-terminal domain mediates WNK1 phase separation
- Phase behavior of the WNK1 CTD is evolutionarily conserved despite sequence divergence
- WNK1 is a molecular crowding sensor and mediator of regulatory volume increase

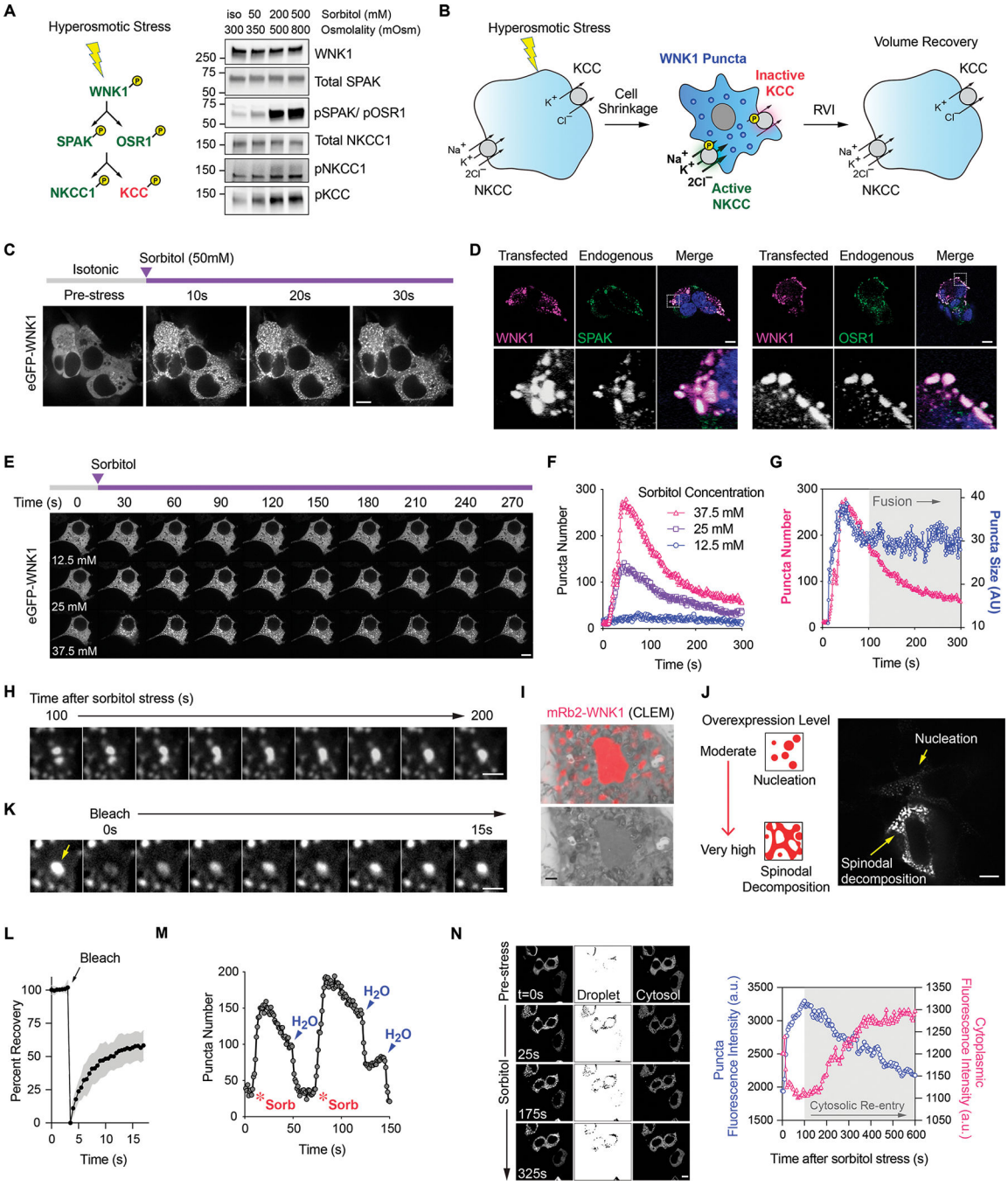

Figure 1. WNK1 forms dynamic liquid-like condensates during hyperosmotic stress.

(A) Left: Phosphorylation-dependent regulation of the WNK1-SPAK/OSR1-NKCC/KCC system. Green phosphoproteins are activated, red are suppressed. Right: Increased endogenous pathway phosphorylation relative to isotonicity (iso), in response to 15min sorbitol stress in HEK cells.

(B) Hyperosmotic stress is associated with WNK1 puncta formation. NKCC1 and KCC are phosphorylated, activating RVI.

(C) Live cell time course of transfected eGFP-WNK1 in HEK cells, subjected to 50mM sorbitol. Representative of >30 experiments.
(D) Fixed IF images of HEK cells transfected with mRuby2-WNK1 subjected to hyperosmotic stress (0.5M sorbitol × 5min), costained for endogenous SPAK and OSR1.
(E-F) Live cell time course of a HEK cell expressing eGFP-WNK1, subjected to a low-level sorbitol stress series (12.5mM-37.5mM), with quantification of puncta number. Representative of 3 experiments.
(G) Comparison of puncta size and number in an eGFP-WNK1 expressing cell subjected to 37.5 mM sorbitol, as shown in (E). 100s into the time course, puncta size stabilized while total number fell, consistent with fusion.
(H) Fusion between two eGFP-WNK1 puncta 100s after 37.5mM sorbitol treatment. Bar= 2μm.
(I) CLEM of a WNK1 condensate in fixed mRuby2-WNK1 transfected cells subjected to 0.1M sorbitol × 15min. Bar= 1μm.
(J) Live cell imaging still of two cells expressing moderate and very high levels of eGFP-WNK1, subjected to 50mM KCl, demonstrating nucleation and spinodal decomposition, respectively. From Video S2.
(K-L) FRAP images and corresponding recovery curve (N=6) of eGFP-WNK1 condensates in cells subjected to 50mM sorbitol. Bar= 2μm.
(M) Reversibility of WNK1 puncta number over time in eGFP-WNK1 transfected cells subjected to osmotic challenges with 37.5 mM sorbitol, followed by H_2O. Bar= 2μm. Representative of 3 experiments.
(N) Quantification of eGFP droplet and cytosolic fluorescence intensity over time in transfected cells.
All bars = 10μm except where indicated. See also Figure S1 and Videos S1–S2.

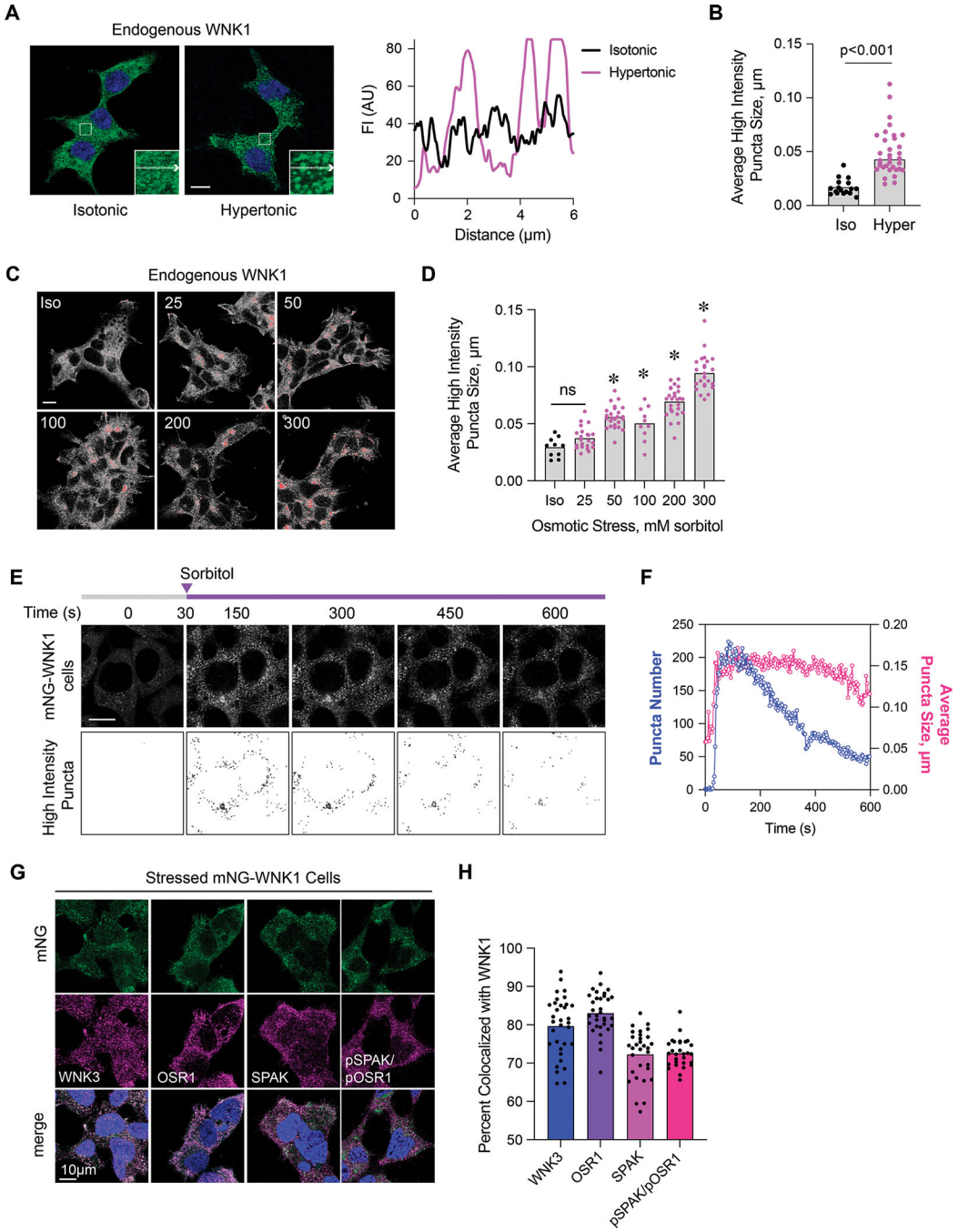

Figure 2. Endogenous WNK1 forms hyperosmotic stress-induced condensates.

(A) Fixed WNK1 IF images in HEK cells under isotonic and hypertonic conditions (300mM sorbitol × 5min). Line scans = fluorescence intensities (FI) along the inset arrows on the left.

(B) Quantification of average high intensity puncta size/confocal field in HEK cells under iso-(n=17 fields) and hypertonic conditions (n=34 fields). p<0.0001 by unpaired T-test. High intensity thresholded signal was kept constant across all conditions analyzed.

(C) Fixed IF images of endogenous WNK1 in HEK cells subjected to various degrees of hypertonic stress (mM sorbitol). Thresholded high intensity signal is shown in red.

(D) Quantification of average high-intensity puncta size/ confocal field in (C). n=10–26 confocal fields per condition; *p<0.0008 by one-way ANOVA, Dunnett's post-hoc test vs isotonic control.

(E-F) Live cell time course of mNG signal in mNG-WNK1 cells subjected to 50mM sorbitol, with quantification of high-intensity puncta number and size (measured across the entire field shown in (E)) over time. Representative of 10 experiments.

(G-H) Colocalization of WNK-SPAK/OSR1 pathway components with mNG-WNK1 in fixed cells subjected to 300mM sorbitol. Colocalization was determined by Mander's M1 overlap coefficient. N=29–33 confocal fields per component.

All bars = 10μm. See also Figure S2–S3 and Video S4.

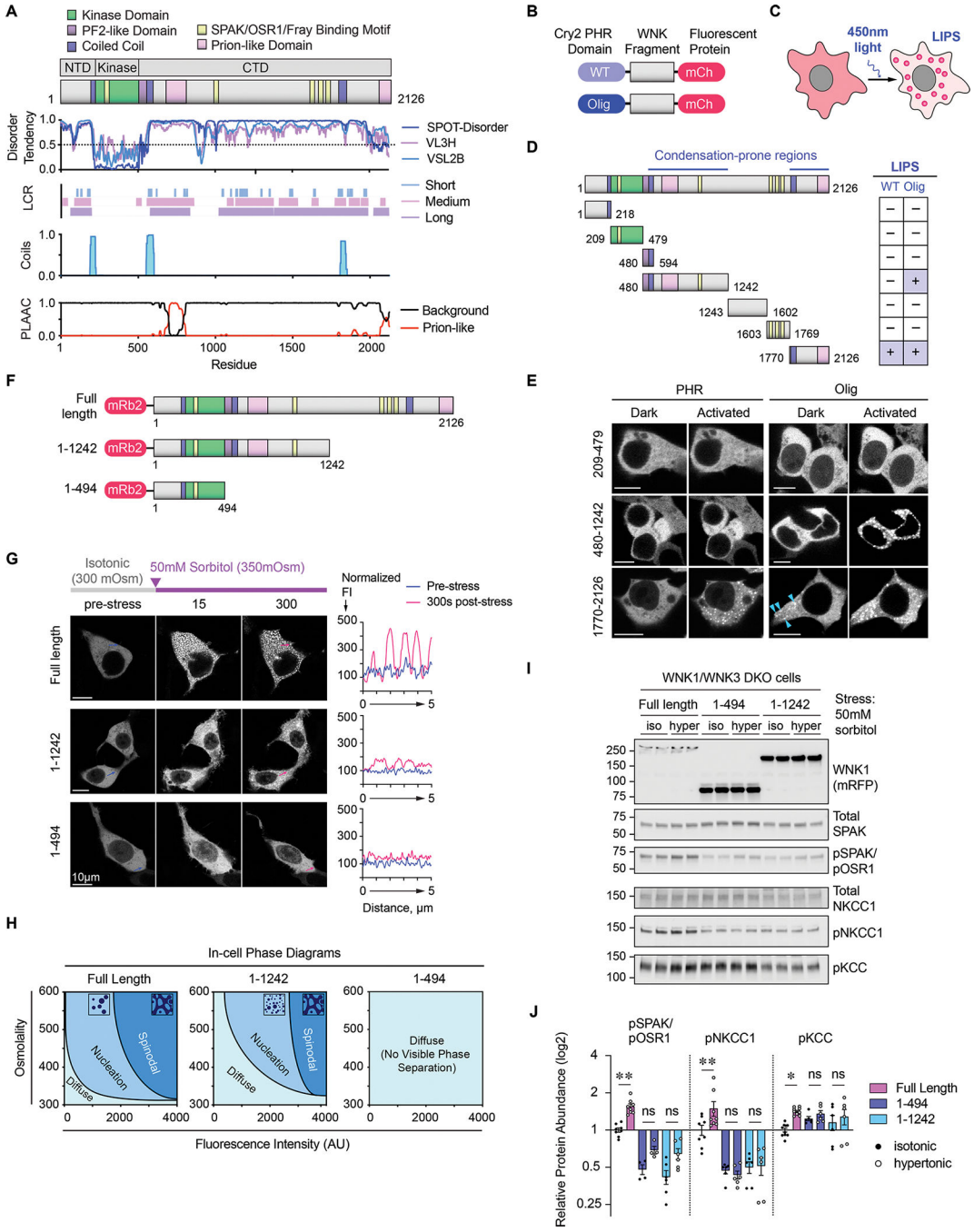

Figure 3. WNK1 phase separation is mediated by its intrinsically disordered CTD.

(A) Mammalian (Rat) WNK1 domain structure, with key domains color-coded on top. The kinase domain is flanked by an N-terminal domain (NTD) and a large C-terminal domain (CTD). Below is a to-scale analysis for protein disorder, low complexity regions (LCR) of short, medium, and long window length, Coiled-coil domains, and Prion-like regions. (B-C) Optogenetic WNK1 constructs, consisting of WT or E490G mutant (“Olig”) PHR domains, fused in-frame to mCherry-tagged WNK1 fragments. Blue light activation of PS-prone fragments triggers light-inducible phase separation (LIPS).

(D) Analysis of PHR-WNK1-mCh fusions. Condensation-prone fragments are depicted with at "+".

(E) Still image examples from live cell LIPS experiments. Two fragments underwent LIPS (480–1242, Olig only; 1770–2126; WT & Olig). 1770–2126 also exhibited spontaneous dark state aggregation when fused to Olig (arrowheads). In contrast, 209–479 (kinase domain) did not undergo LIPS. Bars = 10μm

(F) Full length and truncated N-terminal mRuby2-tagged WNK1 constructs,

(G) Representative live cell images of cells expressing the constructs in (F), pre- and post-osmotic stress. Line scans depict normalized pre- and post-stress fluorescence intensities (FI) along the arrows depicted on the left.

(H) In-cell phase diagrams depicting the phase behavior of the constructs in (F), as a function of FI and extracellular osmolality.

(I-J) SPAK/OSR1/NKCC1/KCC activation in WNK1/WNK3 DKO cells expressing the constructs in (F), under iso- and hypertonic conditions (50mM sorbitol × 30min). p< *0.05 or **0.01 by one-way ANOVA, Sidak's multiple comparison.

See also Figures S4–S5 and Video S5.

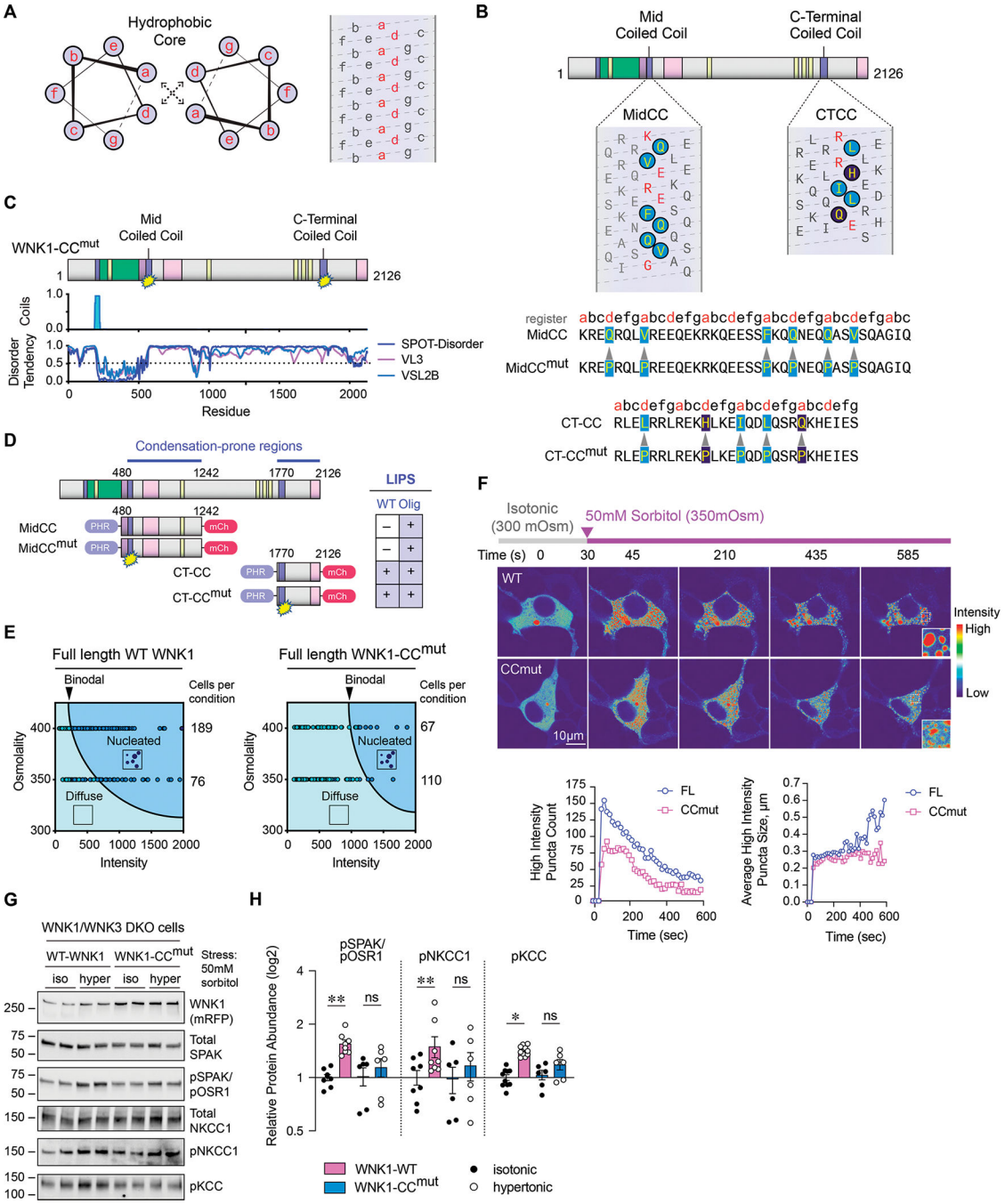

Figure 4. C-terminal coiled coil domains augment WNK1 phase behavior and activity.

(A) Helical wheel and net diagrams of coiled coil (CC) heptad repeats.

(B) Helical net diagram of the MidCC and CTCC domains in rat WNK1. Hydrophobic and Q residues within the *a/d* frame are circled. An "HQ" signature important for CTCC interactions resides within the *a/d* frame. To disrupt CC function, proline substitutions were introduced into the *a/d* register.

(C) WNK1 double CC mutant (WNK1-CC^{mut}). The proline substitutions disrupted predicted CCs without affecting disorder tendency.

(D) Proline mutagenesis of the midCC and CTCC did not affect LIPS in the Cry2-PHR system.
(E) Mutation of the midCC and CTCC in the context of full-length WNK1 (WNK1-CC^{mut}) introduced a rightward shift of the binodal at low levels of hypertonic stress.
(F) PS in sorbitol-stressed wild-type HEK cells expressing mRb2-tagged WT Full-length WNK1 and WNK1-CCmut. Despite similar pre-stress expression levels, the CC mutant formed smaller short-lived condensates. Intensities were pseudocolored using the Thermal lookup table in FIJI.
(G-H) Pathway activation in WNK1/WNK3 DKO cells expressing WT-WNK1 or WNK1-CC^{mut}, under isotonic and hypertonic conditions (50mM sorbitol × 30min). p< *0.05 or **0.01 by one-way ANOVA, Sidak's multiple comparisons test.

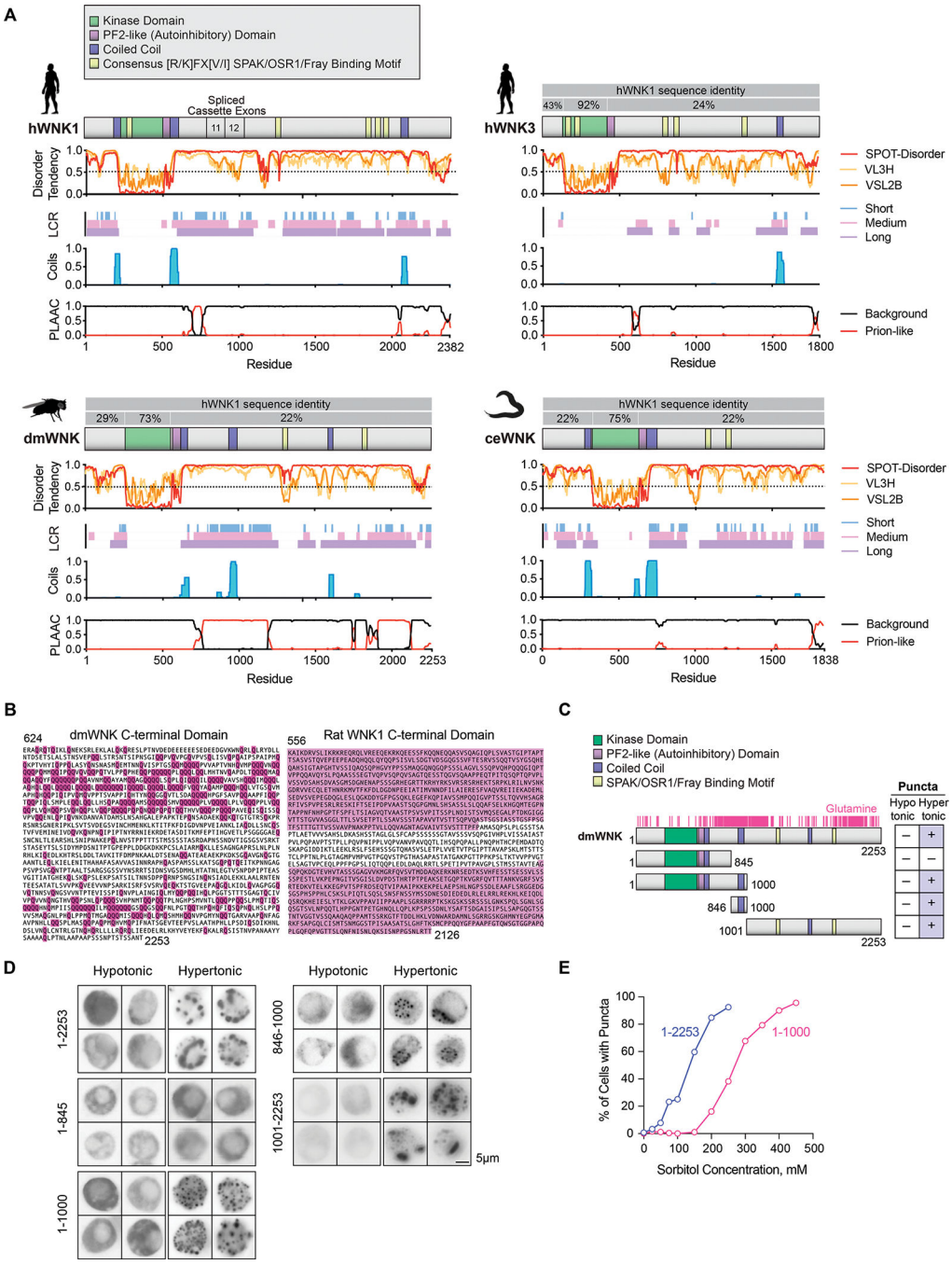

Figure 5. Evolutionary conservation of WNK intrinsic disorder and phase behavior.

(A) Disorder, LCR, CC, and PLD analysis of human WNK1 (hWNK1), human WNK3 (hWNK3), *D. melanogaster* WNK (dmWNK), and *C. elegans* WNK (ceWNK). Sequence identity of hWNK3, dmWNK, and ceWNK versus hWNK1, divided into three regions: the NTD, the kinase domain, and the large C-terminal domain (CTD).

(B) Amino acid sequences of the rat WNK1 and dmWNK CTDs. Glutamines in dmWNK are shown in magenta. Condensation-prone regions in rat WNK1 (Fig 3D) are highlighted in lilac.

(C-D) dmWNK deletion analysis. Diagram of eGFP-tagged dmWNK truncation constructs, with glutamine residues shown in magenta. Apart from dmWNK 1–845, all constructs tested formed puncta during hypertonic stress (376 mOsm).

(E) Compared to full-length dmWNK, dmWNK 1–1000 formed puncta in fewer cells at a given level of hyperosmotic stress. For dmWNK 1–2253, 252–669 cells were assessed per stress condition. For dmWNK 1–1000, 230–659 cells were assessed.

See also Figure S6.

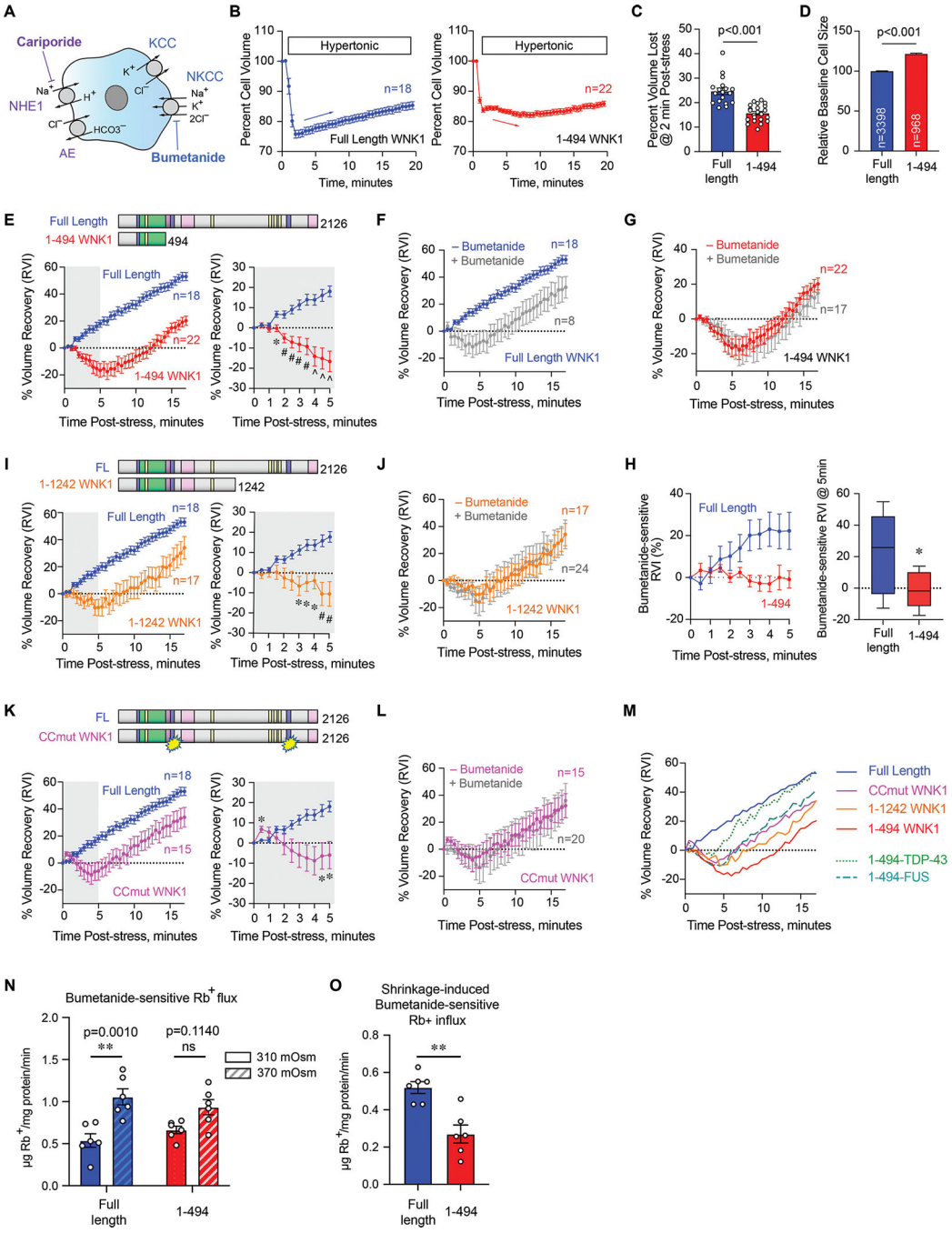

Figure 6. WNK1 CTD augments NKCC1-dependent RVI.

(A) Cariporide-sensitive NHE1/anion exchanger (AE) and bumetanide-sensitive NKCC1/KCC RVI systems. To exclude NHE1-dependent effects, all RVI studies were conducted in the presence of cariporide.

(B) Cell volume changes in WNK1/WNK3 DKO cells, transfected with full-length (FL) or 1-494 WNK1 and subjected to 50mM sorbitol (final = 350mOsm).

(C) DKO cells expressing 1-494 WNK1 exhibit less % volume loss than cells expressing FL WNK1. p<0.001, unpaired T-test.

(D) Cell size measurements in DKO cells expressing FL vs 1-494 WNK1, measured with an ImageStream system. N= # cells analyzed per condition. p<0.001, unpaired T-test.
(E) RVI curves derived from the cell volume measurements in (B), expressed as % volume recovery following cell shrinkage. On the right is a magnification of the gray shaded area on the left graph. *p<0.05, #<0.01, or ^<0.001, repeated measures two-way ANOVA, Sidak's multiple comparison.
(F-G) RVI curves in DKO cells transfected with FL or 1-494 WNK1, +/− Bumetanide.
(H) Bumetanide-sensitive RVI, calculated as the difference between the +/− bumetanide curves in (F) & (G). *p=0.0320 for FL vs 1-494 WNK1 expressing DKO cells @ 5min post stress, unpaired T-test.
(I) RVI curves in DKO cells transfected with 1-1242 WNK1 vs FL WNK1. *p<0.05 or #<0.01, repeated measures two-way ANOVA, Sidak's multiple comparison.
(J) RVI curves in DKO cells transfected with 1-1242 WNK1, +/− Bumetanide.
(K) RVI curves in DKO cells transfected with CC^{mut} WNK1, vs FL WNK1. *p<0.05, repeated measures two-way ANOVA, Sidak's multiple comparison.
(L) RVI curves in DKO cells transfected with CC^{mut} WNK1, +/− Bumetanide.
(M) Summary of mean RVI traces in (E), (I), (K), and for the WNK1 1-494-FUS and -TDP-43 rescue chimeras detailed in Figure S7, presented without error bars. Cells expressing 1-1242 WNK1, CC^{mut} WNK1, or the 1-494 chimeras exhibit an intermediate volume recovery phenotype.
(N) Bumetanide-sensitive Rb+ fluxes in DKO cells transfected with FL or 1-494 WNK1, under near isotonic (310mOsm) or hypertonic (370mOsm) conditions. N=6 sets of fluxes per condition. **p=0.0010 by two-way ANOVA, Tukey's multiple comparison.
(O) Shrinkage-induced Bumetanide-sensitive Rb flux in DKO cells transfected with FL WNK1 or 1-494 WNK1. N=6 sets of flux measurements per condition. **p=0.0015 by unpaired T-test.
See also Figures S5 and S7.

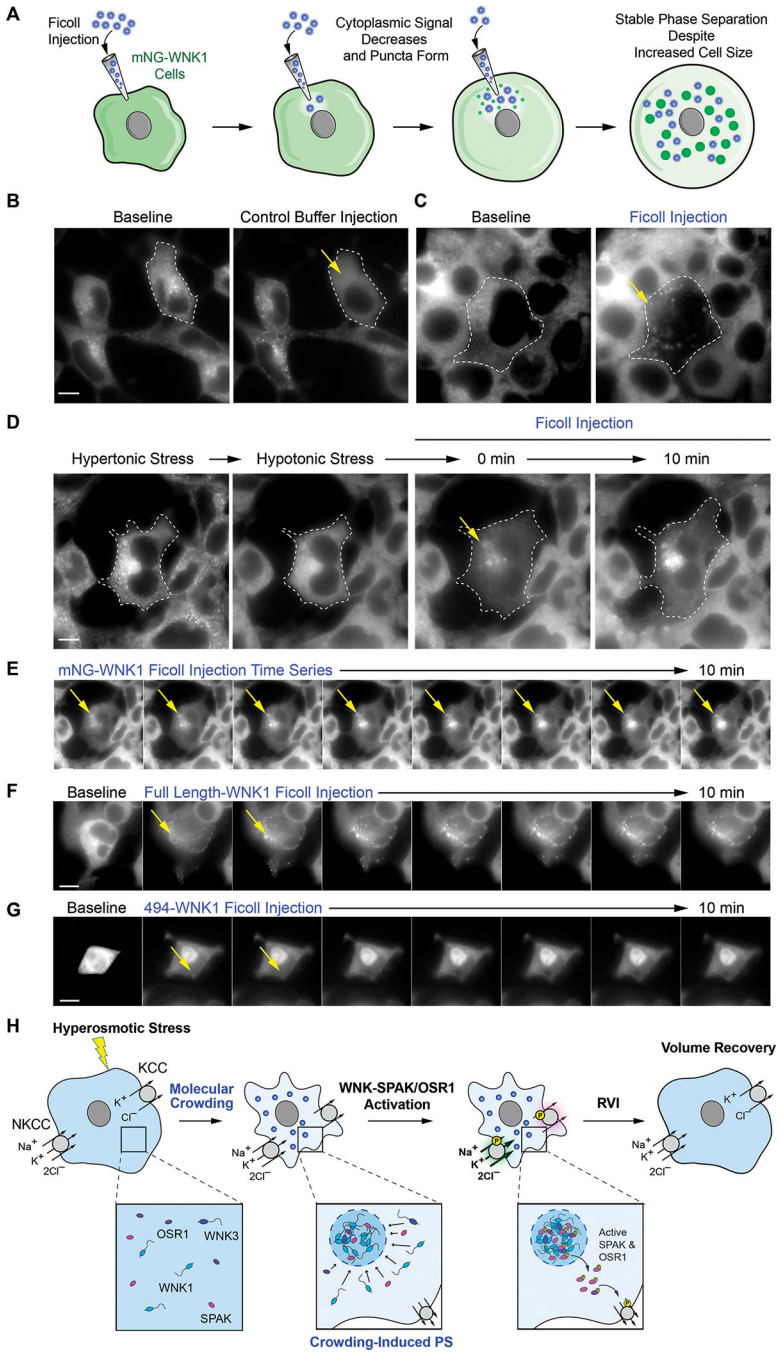

Figure 7. WNK1 is a molecular crowding sensor.

(A) Ficoll microinjection experiment.

(B) Effect of “KH” K+ Acetate/HEPES vehicle control buffer microinjection into mNG WNK1 cells

(C) Microinjection of Ficoll-containing KH buffer increased mNG-WNK1 puncta formation.

(D) mNG-WNK1 cells subjected to hypertonic stress (50mM KCl), hypotonic cell swelling (1:1 water in KH buffer), followed by Ficoll microinjection.

(E) 10min timecourse following Ficoll injection. Crowding agent induced localized long-lived puncta formation.
(F) Ficoll injection into HEK-293 cells (WT background) expressing mRb2 full length WNK1 induced widespread sustained puncta formation over a 10min timecourse.
(G) Cytosolic Ficoll injection into HEK-293 cells expressing mRb2-1-494 WNK1 resulted in no visible PS and dilution of cytoplasmic signal. The construct partially distributes into the nucleus; fluorescence intensity of this fraction remained unchanged over 10min.
(H) WNK-SPAK/OSR1 activation during hyperosmotic stress. Hyperosmotic stress causes cell shrinkage and crowding. This triggers PS of the WNK-SPAK/OSR1 pathway. Pathway localization within condensates favors SPAK/OSR1 phosphoactivation. Material leaves the WNK condensates, permitting phosphorylation of NKCC1 and the KCCs at the plasma membrane, resulting in net ion influx and RVI.
All bars = 10μm. See also Video S7.

Key resources table

REAGENT or RESOURCE	SOURCE	IDENTIFIER
Antibodies		
Rabbit Anti-WNK1	Atlas	RRID: AB_2683935
Rabbit Anti-WNK1	Atlas	RRID: AB_2679690
Rabbit Anti-WNK3	Millipore Sigma	RRID: AB_10807990
Rabbit Anti-WNK3	Millipore Atlas	RRID: AB_2686850
Rabbit Anti-OSR1	Atlas	RRID: AB_1079540
Rabbit Anti-SPAK	Cell Signaling Technology	RRID: AB_2196951
Rabbit Anti-phospho-SPAK (Ser373) / phospho-OSR1 (Ser325)	Millipore Sigma	RRID: AB_11205577
Guinea Pig Anti-NKCC1	(This paper)	N/A
Rabbit Anti-pNCC (Thr58)	Jan Loffing (Sorensen et al 2013)	N/A
Rabbit Anti-pKCC (Thr1007)	PhosphoSolutions	RRID: AB_2716769
Mouse Anti-mNeonGreen [32F6]	Bulldog Bio	RRID: AB_2827566
Rabbit Anti-tRFP	Evrogen	RRID: AB_2571743
Rabbit Anti-GAPDH	Cell Signaling Technology	RRID: AB_561053
Mouse Anti-EEA1	BD Biosciences	RRID: AB_397829
Mouse Anti-LAMP2	DS Hybridoma Bank	RRID: AB_528129
Mouse Anti-gamma-adaptin (AP-1)	BD Transduction Lab	RRID: AB_397768
Rabbit Anti-Clathrin Heavy Chain	Abcam	RRID: AB_2083165
Rabbit Anti-EMC2	Proteintech	RRID: AB_2750836
Mouse Anti-TIAR	(Daigle et al., 2016)	N/A
Rabbit Anti-eIF4e	Bethyl Laboratories	RRID: AB_2246256
Rabbit Anti-DCP2	Bethyl Laboratories	RRID: AB_10555903
Peroxidase AffiniPure Goat Anti-Rabbit IgG (H+L)	Jackson ImmunoResearch	RRID: AB_2313567
Peroxidase AffiniPure Goat Anti-Guinea Pig IgG (H+L)	Jackson ImmunoResearch	RRID: AB_2337402
Peroxidase AffiniPure Goat Anti-Mouse IgG (H+L)	Jackson ImmunoResearch	RRID: AB_10015289
Goat Anti-Rabbit Alexa 488	Invitrogen	RRID: AB_143165
Donkey Anti-Rabbit Cy3	Biolegend	RRID: AB_893532
Goat Anti-Mouse Alexa 568	Invitrogen	RRID: AB_2534072
Bacterial and virus strains		
E.coli TOP10	Thermo/ Invitrogen	Cat# C4040
E.coli INV110	Thermo/ Invitrogen	Cat# C7171
Biological samples		
Chemicals, peptides, and recombinant proteins		
.5M EDTA	Lonza	Cat# 51234; CAS:610769-35-2
.5M Tris HCl pH 6.8	BioRad	Cat# 1610799
10% SDS	Teknova	Cat# S0289

REAGENT or RESOURCE	SOURCE	IDENTIFIER
16% Paraformaldehyde	Electron Microscopy Sciences	Cat# 15710
1M Tris pH 8	Invitrogen	Cat# 15568025
2-Mercaptoethanol	Sigma	Cat# M7522; CAS:60-24-2
2-Propanol	Fisher	Cat# A426P-4; CAS:67-63-0
200 Proof Ethanol	Decon Laboratories Inc.	Cat# 2705; CAS:64-17-5
4–20% Criterion™ TGX™ Precast Midi Protein Gel	BioRad	Cat# 5671095
4–20% Mini-PROTEAN® TGX Precast Protein Gels	BioRad	Cat# 4561096
Ammonium Chloride	Sigma	Cat# 09718; CAS:12125-02-9
Ampicillin	Sigma	Cat# A9518; CAS:69-52-3
Antibody Diluent	Life Technologies	Cat# 003118
Blotting-Grade Blocker	BioRad	Cat# 1706404
Bumetanide	Cayman Chemical Company	Cat# 14630
Cariporide	Sigma	Cat# SML1360; CAS: 159138-80-4
Clarity Max Western ECL Substrate	BioRad	Cat# 1705062
Clarity Western ECL Substrate	BioRad	Cat# 1705061
Coomassie Brilliant Blue R-250 Staining Solution	BioRad	Cat# 1610436
D-Sorbitol	Sigma	Cat# S7547; CAS:50-70-4
Deoxycholate	Sigma	Cat# D2510; CAS:83-44-3
DMEM	Gibco	Cat# 11995065
DPBS with Ca/Mg	Lonza	Cat# 17-513F
EGTA	ThermoFisher	Cat# 409910250; CAS: 67-42-5
FBS	Gemini	Cat# 100-500
Ficoll	Sigma	Cat# F4375; CAS: 26873-85-8
Fish Gelatin	Biotium	Cat# 22010
Glacial Acetic Acid	Millipore	Cat# AX0073; CAS:64-19-7
Glycerol	Sigma	Cat# G5516; CAS:56-81-5
Glycine	Acros Organics	Cat# AC120072500; CAS:56-40-6
HEPES	Fisher	Cat# AC172572500; CAS:7365-45-9
L-Glutamine	Gibco	Cat# 25030081
LB Agar	BD	Cat# 244510
LB Broth	BD	Cat# 244610
LE Quick Dissolve Agarose	GeneMate	Cat# E-3119-500; CAS:9012-36-6
Leibovitz's L-15 Medium	Gibco	Cat# 21083027
Lipofectamine 3000	ThermoFisher	Cat# L3000
Opti-MEM	ThermoFisher	Cat# 31985
Pen-Strep	MP Biomedicals Inc.	Cat# 1670249
Pepstatin	Sigma	Cat# P5318; CAS:26305-03-3
Phenylmethanesulfonyl fluoride (PMSF)	Sigma	Cat# P7626; CAS:329-98-6
PhosStop	Roche	Cat# 04906837001

REAGENT or RESOURCE	SOURCE	IDENTIFIER
Pierce Bovine Serum Albumin Standard Ampules	ThermoFisher	Cat# 23209
Protease Inhibitor	ThermoFisher	Cat# A32955
QuickExtract DNA extraction solution	Lucigen	Cat# QE09050
SDS powder	Fisher	Cat# BP8200500; CAS:151-21-3
Sodium Chloride	Sigma	Cat# S9625; CAS:7647-14-5
SYBR Safe DNA Gel Stain	ThermoFisher	Cat# S33102
ToPro3	Invitrogen	Cat# T3605
Trans-Blot Turbo Midi 0.2 μm Nitrocellulose Transfer Packs	BioRad	Cat# 1704159
Triton X-100	Sigma	Cat# T9284; CAS:9036-19-5
Trypsin	Gibco	Cat# 25300054
Critical commercial assays		
HiSpeed Plasmid Midi Kit	Qiagen	Cat# 12643
QIAquick Gel Extraction Kit	Qiagen	Cat# 28704
QIAprep Spin Miniprep Kit	Qiagen	Cat# 27106
Pierce BCA Protein Assay Kit	ThermoFisher	Cat# 23225
Deposited data		
Raw and analyzed data	Mendeley	doi: 10.17632/6266thh95j.1
Experimental models: Cell lines		
Human: HEK-293 [female]	American Type Culture Collection (AtCC)	CRL-1573
Human Gene edited cell line: HEK-293T WNK1 KO clone 7	This paper and Roy et al., 2015 (PMID: 25477473)	N/A
Human Gene edited cell line: HEK-293 WNK1/WNK3 DKO clone 3.5.4	This paper	N/A
Human Gene edited cell line: HEK-293 mNG-WNK1 clone 11	This paper	N/A
Human: GBM43 glioma [male]	C. David James	N/A
Human: U-2 OS [female]	ATCC	HTB-96
D. melanogaster: Cell line S2 Gal4 [male]	A. Rothenfluh (J Neurosci 35: 15396)	N/A
Experimental models: Organisms/strains		
Mouse: FVB.Cg-Slc12a2tm1Ges/Mmjax	G. Shull (PMID: 10480906)	034262-JAX
Oligonucleotides		
sgRNA Guide oligo: hWNK1 exon 1 (for WNK1 KO) 5’ GCACTCTGCGGGACAGCCGC	Roy et al., 2015 (PMID: 25477473)	N/A
sgRNA Guide oligo: hWNK3 exon 2 (for WNK3 KO; guide 3.5) 5’ GCCTTAATTCTCTCATCTTT	This paper	N/A
sgRNA Guide oligo: hWNK1 exon 1 (for WNK1 mNG knockin) 5’ AGCGAACCGACCATGTCTGG	This paper	N/A
WNK1 mNG knockin HDR template: 5’ homology arm fwd primer 5’ CCTGCAGCCCAGTCCTCTAGGTCTCCTCTCCTCT	This paper	N/A

REAGENT or RESOURCE	SOURCE	IDENTIFIER
WNK1 mNG knockin HDR template: 5' homology arm rev primer 5' CTCACCATGGTCGGTTCGCT	This paper	N/A
WNK1 mNG knockin HDR template: 3' homology arm fwd primer 5' AGGCTCCATGTCTGGCGGC	This paper	N/A
WNK1 mNG knockin HDR template: 3' homology arm rev primer 5' TTCGAGCTCATGACCTTCACCAC	This paper	N/A
Recombinant DNA		
pcDNA3.1(+)	Thermo/ Invitrogen	Cat# V790-20
pcDNA3.1_rWNK1-S-G-HA-eGFP	Boyd-Shiwarski et al., 2018 (PMID:29287322)	N/A
pcDNA3.1_rWNK1-S-G-HA-mRuby2	Boyd-Shiwarski et al., 2018 (PMID:29287322)	N/A
pcDNA3.1_mRuby2-rWNK1-S-G	This paper	N/A
pcDNA3.1_mRuby2-rWNK1 (1-494)	This paper	N/A
pcDNA3.1_mRuby2-rWNK1 (1-1242)	This paper	N/A
pcDNA3.1_mRuby2-rWNK1-S-G DoubleCCmut [Q571P/ V575P/ F589P/ Q592P/ Q596P/ V599P/ L1820P/ H1827P/ 11831P/ L1834P/ Q1838P]	This paper	N/A
pcDNA3.1_mRuby2-SPAK	This paper	N/A
pcDNA3.1_eGFP-SPAK	This paper	N/A
pcDNA3.1_mRuby2-rWNK1 (1-494)-FUS_LCD (1-267)	This paper	N/A
pcDNA3.1_mRuby2-rWNK1 (1-494)-TDP-43_LCD (273-414)	This paper	N/A
px330	Gift from Feng Zhang	RRID:Addgene_42230
px330_sgRNA-hWNK1	Roy et al., 2015 (PMID: 25477473)	N/A
px330_sgRNA-hWNK3.5	This paper	N/A
px459	Gift from Feng Zhang	RRID:Addgene_62988
px459_sgRNA-hWNK1	This paper	N/A
pUC18_mNG-hWNK1_HDRT	This paper	N/A
pCry2PHR-mCherryN1	Kennedy et al., 2010 (PMID: 21037589)	RRID:Addgene_26866
PHR_1.05: pCry2PHR-rL-WNK1 (1-218)-mCh	This paper	N/A
PHR_1.06: pCry2PHR-rL-WNK1 (209-479)-mCh	This paper	N/A
PHR_1.07: pCry2PHR-rL-WNK1 (480-594)-mCh	This paper	N/A
PHR_1.10: pCry2PHR-rL-WNK1 (1243-1602)-mCh	This paper	N/A
PHR_1.11: pCry2PHR-rL-WNK1 (1603-1769)-mCh	This paper	N/A
PHR_1.12: pCry2PHR-rL-WNK1 (1770-2126)-S-G-mCh	This paper	N/A
PHR_1.20: pCry2PHR-rL-WNK1 (1770-2126)-S-G-mCh [L1820P/ H1827P/ I1831P/ L1834P/ Q1838P/ S2120G]-mCh	This paper	N/A
PHR_1.21: pCry2PHR-rL-WNK1 (480-1242)-mCh	This paper	N/A
PHR_1.22: pCry2PHR-rL-WNK1 (480-1242)-mCh [Q571P/ V575P/ F589P/ Q592P/ Q596P/ V599P]	This paper	N/A
pHRS	PNABio	Cat# RV03
pHRS-hWNK3.5_reporter	This paper	N/A

REAGENT or RESOURCE	SOURCE	IDENTIFIER
pEGFP-C2	Clontech	Cat# 6083-1
pUC18	ThermoFisher	Cat# SD0051
pCry2Olig-mCherry	Taslimi et al., 2014 (PMID: 25233328)	RRID:Addgene_60032
Olig_2.05: pCry2Olig-rL-WNK1 (1-218)-mCh	This paper	N/A
Olig_2.06: pCry2Olig-rL-WNK1 (209-479)-mCh	This paper	N/A
Olig_2.07: pCry2Olig-rL-WNK1 (480-594)-mCh	This paper	N/A
Olig_2.21: pCry2Olig-rL-WNK1 (480-1242)-mCh	This paper	N/A
Olig_2.10: pCry2Olig-rL-WNK1 (1243-1602)-mCh	This paper	N/A
Olig_2.11: pCry2Olig-rL-WNK1 (1603-1769)-mCh	This paper	N/A
Olig_2.12: pCry2Olig-rL-WNK1 (1770-2126)-S-G-mCh	This paper	N/A
Olig_2.20: pCry2Olig-rL-WNK1 (1770-2126)-S-G-mCh [L1820P/ H1827P/ I1831P/ L1834P/ Q1838P/ S2120G]-mCh	This paper	N/A
Olig_2.21: pCry2Olig-rL-WNK1 (480-1242)-mCh	This paper	N/A
Olig_2.22: pCry2Olig-rL-WNK1 (480-1242)-mCh [Q571P/ V575P/ F589P/ Q592P/ Q596P/ V599P]-mCh	This paper	N/A
pGEM T-Easy	Promega	Cat# A1360
pAC5 STABLE2 Neo	Sci Reports 2011;1:75 (PMID: 22355594)	RRID:Addgene_32426
pAc5-GFP:T2A:HsSPAK_D210A	This paper	N/A
pAC5-GFP-dmWNK (1-2253):T2A:HsSPAK_D210A	This paper	N/A
pAC5-GFP-dmWNK (1-845):T2A:HsSPAK_D210A	This paper	N/A
pAC5-GFP-dmWNK (1-1000):T2A:HsSPAK_D210A	This paper	N/A
pAC5-GFP-dmWNK (846-1000):T2A:HsSPAK_D210A	This paper	N/A
pAC5-GFP-dmWNK (1001-2253):T2A:HsSPAK_D210A	This paper	N/A
Software and algorithms		
DISPROT–VSL2B	Obradovic et al., 2005 (PMID:16187360)	http://original.disprot.org/metapredictor.php
DISPROT–VL3H	Peng et al., 2005 (PMID: 15751111)	https://www.dabi.temple.edu/external/disprot/predictor.php
SPOT-Disorder	Hanson et al., 2017 (PMID: 28011771)	https://sparks-lab.org/server/spot-disorder/
SEG	Wooton, 1994 (PMID: 7952898)	http://mendel.imp.ac.at/METHODS/seg.server.html
NCOILS	Lupas et al., 1991 (PMID: 2031185)	https://npsa-prabi.ibcp.fr/cgi-bin/npsa_automat.pl?page=/NPSA/npsa_lupas.html
MARCOIL	Delorenzi et al., 2002 (PMID:12016059)	https://toolkit.tuebingen.mpg.de/tools/marcoil
ProtParam (ExPASy)	Gasteiger et al., 2005	https://web.expasy.org/protparam/
PLAAC	Lancaster et al., 2014 (PMID: 24825614)	http://plaac.wi.mit.edu/
Fiji	Schindelin et al., 2012 (PMID:22743772)	https://imagej.net/Fiji
LAS X	Leica Microsystems	Version 3.5.5

REAGENT or RESOURCE	SOURCE	IDENTIFIER
Other		
Biocoat coverslips	Corning	Cat# 354086
Super frost Plus Microscope Slides	Fisher	Cat# 12-550-15
ProLong Glass	Invitrogen	Cat# P36980
Glass bottom dish, PDL coated	MatTek Corporation	Cat# P35GC-1.5-10-C